ADVANCED ELECTROSTATIC TRANSDUCERS: FOR ULTRA LOW-POWER SENSING AND HIGH WORK DENSITY ACTUATION

by

Amin Abbasalipour

APPROVED BY SUPERVISORY COMMITTEE:

____
Siavash Pourkamali, Chair

____
Jeong-Bong Lee

____
Gil S. Lee

____
Majid Minary

This dissertation is dedicated to my family, who inspired me to pursue my dreams with their continuous support and sacrifice.

ADVANCED ELECTROSTATIC TRANSDUCERS: FOR ULTRA LOW-POWER SENSING AND HIGH WORK DENSITY ACTUATION

by

AMIN ABBASALIPOUR, MS

DISSERTATION
Presented to the Faculty of
The University of Texas at Dallas
in Partial Fulfillment
of the Requirements
for the Degree of

DOCTOR OF PHILOSOPHY IN
ELECTRICAL ENGINEERING

THE UNIVERSITY OF TEXAS AT DALLAS
August 2020

ACKNOWLEDGMENTS

First and foremost, I would like to express my deepest appreciation and gratitude to my PhD advisor and mentor Dr. Siavash Pourkamali for his guidance and invaluable support. With his unique intellect and his unwavering conviction in the value of scientific intuition, he has truly inspired me. I would also like to thank my committee members Dr. J.B. Lee, Dr. Gil Lee and Dr. M. Minary for their insightful comments and suggestions.

I would like to acknowledge my friends and colleagues Dr. Varun Kumar, Dr. Mohamad Mahdavi, Dr. Alireza Ramezany, Dr. Vahid Gharadaghi, Sarah Farahani, Sepehr Sheikhlari, Prithviraj Palit, Hamed Nikfarjam for their valuable discussions and cooperation. I also want to thank the cleanroom staff at The University of Texas at Dallas who did their best to keep the equipment running all the time.

Last but not least, I wish to thank my dear parents and my brother, who have made great sacrifices for me to be where I am. They have been a constant source of emotional support and inspiration for many years away from family.

April 2020

ADVANCED ELECTROSTATIC TRANSDUCERS: FOR ULTRA LOW-POWER SENSING AND HIGH WORK DENSITY ACTUATION

Amin Abbasalipour, PhD
The University of Texas at Dallas, 2020

Supervising Professor: Siavash Pourkamali

Over the last few decades, various micro-electromechanical (MEMS) transducers utilizing different actuation and sensing mechanisms have been demonstrated and many of them successfully implemented for wide variety of applications. Although conventional sensors and actuators developed based on MEMS technology address most of the applications, this dissertation focuses on exploring novel approaches to improving the performances of such devices.

Among the MEMS sensors, MEMS accelerometers are one of the most successfully commercialized devices implemented for various consumers, industrial, military and biomedical applications. In most cases for the MEMS accelerometer, an analog front end is needed for reading, processing, and analog to digital conversion of the sensor output. Typically, the analog front end is responsible for most of the power consumption of the whole sensor. The proposed effort in this dissertation aims at development of a new class of digitally operating MEMS accelerometers allowing significant power reduction by eliminating the need for the analog front-end.

Any electrically powered system with mechanical moving parts utilizes actuators converting electrical energy into mechanical motion. Examples of such includes robotic systems, unmanned vehicles, precision positioning systems, optical systems (e.g. cameras and LIDARs), and medical devices. Piezoelectric actuators are the preferred choice for high precision systems with displacements in the microns range. While piezoelectric actuators are highly power efficient and can output large amounts of force, reaching hundreds of microns of displacement, would require a large piezoelectric element, or non-monolithic integration of a levering mechanism trading excess force for much needed displacement. On the other hand, Electrostatic actuators provide similar or better power efficiency as piezoelectrics, while having much softer structures. Arrayed cellular electrostatic actuators enabled by state-of-the-art MEMS technology, offering displacements in the tens to hundreds of microns while being highly power efficient, compact, and lightweight.

TABLE OF CONTENTS

LIST OF FIGURES

LIST OF TABLES

CHAPTER 1

INTRODUCTION

1.1 MEMS Transducers

Generally, Micro-Electro-Mechanical Systems (MEMS) are micro scale mechanical or electro-mechanical components embedded in semiconductor chips which are made by using micro-fabrication techniques. MEMS transducer is a device that converts energy from one domain to another domain for purposes of measurement or control. Due to the advantages of MEMS transduces such as their low power consumption, low cost of fabrication, size, and easy integration with CMOS technology, MEMS transducers have been received a lot of interest in both researches and industries during the last decades.

Transducers can be categorized into two groups, sensors, and actuators. Actuators are transducers that are used in moving or controlling a system, such as controlling the position of a mobile microstructures. Sensors, on the other hand, are transducers used to measure a physical quantity such as pressure sensors, accelerometers, gyroscopes, etc. In addition to different applications of MEMS transducers, sensors typically have small amount of input power required for the operation of devices. However, actuators are mostly high-input power devices. The combination of the two can be used to monitor and control a physical system or process [1].

There are various means by which one can implement these transducers in actuating or sensing [1][3]. The MEMS sensing can be mostly done by the following methods. Resistive sensing is a method in which the change in the electrical resistance is measured. There are two types of resistive sensing. The most famous one, which is also commercialized, is called Piezoresistive sensing. Exerting stress on a material can cause the electrical resistance of the said material to change and this change can be used as a sensing method. This effect is particularly significant in some semiconductors. Another type of resistive sensing is Magnetoresistive sensing. When subjected to a magnetic field a material's electrical resistance can changes if so the material is called magnetoresistive [4]. A different form of sensing called thermo resistive sensing. Most electrically resistive materials, when subjected to an environmental temperature change, undergo a resistance change as well which can be used as a means for sensing. There is also capacitive sensing. In this case, the sensor is designed so that the measurand causes some portion of the capacitor assembly to move. The input motion alters the capacitance, changing the voltage difference between conductors which can be easily detected and measured. Piezoelectric sensing is a popular form of sensing. If we squeeze or press a piezoelectric material, the material produces an electric charge. The effect is reversible—if we apply a charge to a piezoelectric material, the material mechanically deforms in response. Therefore, these materials can be used in sensing as well as actuating. Another method of sensing is resonant sensing in which the resonance frequency of the device is monitored and changes in the resonance frequency can be utilized as a sensing mechanism. Thermoelectric sensing is a way that measures voltage difference between two materials. In thermoelectric materials this flow of energy creates a voltage effect distributed between the two points. The effect is reversible—if we apply a voltage difference across a thermoelectric material a temperature difference can be created. Magnetic sensing is a different method of sensing. The principle is either the change in the energy stored in the magnetic field or charged particle interacting in the magnetic field.

Similar to sensing, there are numerous ways of actuation [1][5]. Capacitive actuation is one of the methods. In sensing, an input motion produces an output voltage. In actuation, an input voltage produces an output motion. There is also piezoelectric actuation. As mentioned before in sensing, if we apply a charge to a piezoelectric material, the material mechanically deforms in response which is the principle of the piezoelectric actuation. A lot of actuators are based on thermo-mechanical actuation. Bimetallic actuation is based on the thermal mismatch which applies stress in thin films, which could result in the bending of a substrate. Essentially a bimetallic actuator actively controls thermal mismatch stress in order to bring about deformation at will, and hence, actuation. Another method is thermopneumatic actuation which relies on the large expansion of a fluid as it changes phase from liquid to gas. When heated, a trapped fluid in the actuator begins to change phase from liquid to vapor. As the vapor has a much lower density than the liquid, the fluid expands and forces the walls of the space containing the fluid to expand, much like blowing up a balloon, causing the actuator motion. Another form of actuation is hot arm actuation. Hot arm actuators make use of the expansion of material when heated. There are a narrow arm and a wider arm in the structure. When electrical current passes through the device the narrow arms tend to heat up more due to higher electrical resistance and this, in turn, creates more expansion in the narrower arm comparing to the wider arm. The different rates of expansion cause the actuator to bend. Magnetic actuation is another form. Magnetic transduction is one of the physical principles that can be used for either sensing or actuation, though not at the same time.

1.2 MEMS Accelerometer

During the last few decades, MEMS accelerometers have been developed extensively in sensor applications. They can be implemented in numerous capacities including smartphones [6], traction and vehicle stability control [7], air bag deployment [8], Detection of Driving Events [9], seismic-data acquisition [10] medical applications such as hearing aids [11] heart and lung monitoring [12].

Various forms of these sensors can be found in the field, be it a single axis analog output accelerometer or a high-end smart sensor with digital output. Variety of sensing and transduction mechanisms has been established. Most used approaches and detection mechanisms include capacitive [13][14], piezoelectric [15][16], piezoresistive [17][18] and electron tunneling readout [19]. One of the most successful methods is capacitive sensing in which there are movable electrodes attached to a suspended mass and fixed electrodes attached to the substrate. The change in capacitance is measured when the device is subjected to external acceleration. Among the benefits of the capacitive approach is simple structure, high sensitivity, low temperature sensitivity, and low-power dissipation [20].

Development of the Internet of things and the need for wireless sensors makes power consumption (especially in the front-ends) a significant factor in accelerometers. With aggressive power reduction in digital electronics in recent years, MEMS sensors remain one of the most power-hungry components in integrated systems. This limits the application of these sensors since they may be needed to be installed where access to power source is restricted. For instance, accelerometers have been used in monitoring the physical activity of human beings [21][22]. High power consumption in this case either means frequent charging of the device or having a bulky device with reduced wear ability due to a larger battery; both of which result in a decrease in the comfort level of the patient [23]. Lee et al have reported a wireless sensor network (WSN) for monitoring the health and performance of motors. WSN consist of MEMS sensors, two signal processors, and the communication modules. The total nominal power consumption of the WSN is as high as 35mW, out of which close to 62% (21.6mW) is the power required for operation of the MEMS sensor [24], which includes the analog front end needed for reading, processing, and the analog to digital conversion of the sensor output [25]. Consequently, removing analog front-end significantly alternates the simplicity of the device and in turn improving the power consumption of an accelerometer (Figure 1.1).

This calls for a paradigm shift in MEMS sensor design moving from analog sensors towards sensors with direct digital operation/output. Not only does direct digital output enhances power consumption, but it also benefits the size of the device and the noise produced in the front ends. For example, Kobayashi et al have demonstrated a piezoelectric accelerometer connected to an array of CMOS converters with satellite capacitors. The on-state and off-state of CMOS inverters correspond to logic ‘0’ and ‘1’. The number of on-state CMOS inverters responses to increasing the acceleration applied to the piezoelectric accelerometer [26].

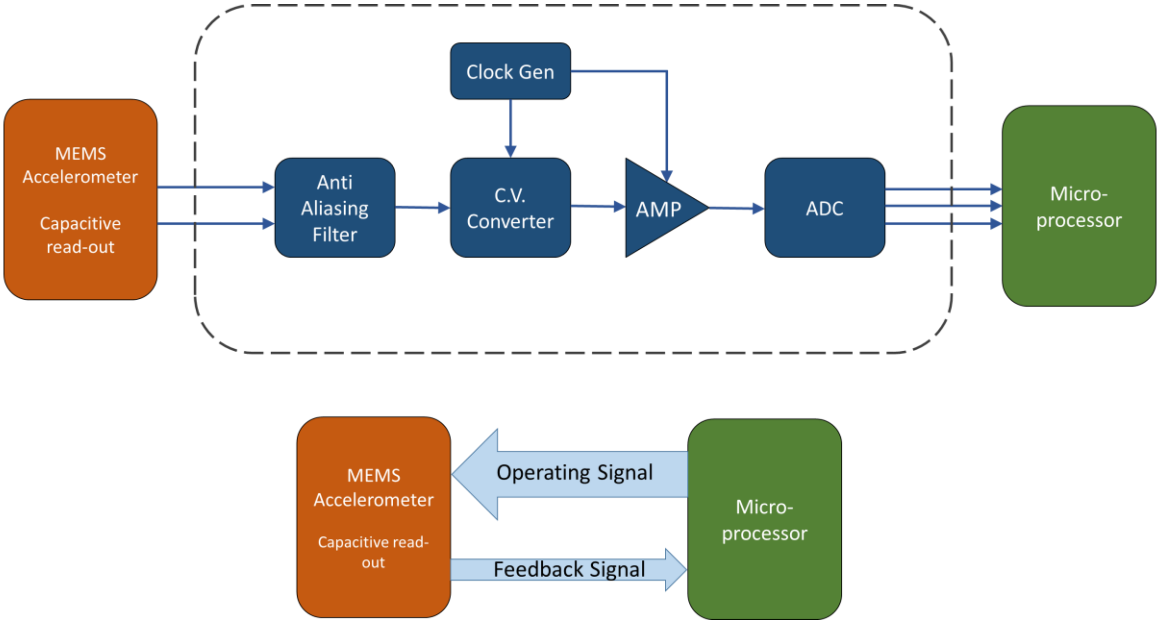

Figure 1.1.(a). Simplified schematic of the conventional MEMS capacitive read out accelerometer along with the analog front end required for readout, (b). Simplified schematic of the Digitally operating MEMS Accelerometer.

The concept of low power tunable acceleration switches as digital MEMS accelerometers and a 2-bit prototype have been previously demonstrated [27][28]. Later on, we have proposed the higher bits of resolution as 5-bit digitally operating accelerometer to demonstrate the higher resolution along with power reduction [29]. In an effort to provide a direct digital output as well as dramatically reduced power consumption of MEMS inertial sensors, we have demonstrated a fully digital 8-bit MEMS accelerometer by digitally operating a tunable MEMS acceleration switch. In this manner, a microprocessor has been applied to run the binary search in order to perform the acceleration detection. Also, the frequency/time response of the device have been studied along with the reliability of the device.

1.3 MEMS Actuators

Micromachined actuators with large rage of displacement and high work performance are of great demand in the recent days. Application for such electromechanical actuators is diverse ranging over various research and commercial endeavors in micro-robotics[30], surgical/medical micro-devices[31], precision micro/nano-positioning systems and instrumentation[32], as well as optical systems (miniature integrated camera lenses and LIDARs)[33], and super high frequency (SHF) scanning electrical antenna[34]. In the past few decades, various actuators have been developed to meet the demand of different applications mentioned and they are typically driven by electrostatic, piezoelectric, and electromagnetic methods but each of them has its own limitation. Electromagnetic actuators typically enable high output force and large displacement stroke, but they are known to consume high power and are also usually have large footprint [35]. Piezoelectric actuators on the other hand provide high output force but they offer very low stroke and are also not very easy to fabricate [36],[37]. Compared to the other methods, designs with electrostatic actuators offer higher speed response and low power consumption but it has been challenging to design them in a way that can provide high displacement and force at the same time [38]. Several electrostatic actuator designs have been reported to provide in plane translation. Self-aligned vertical comb drive actuator had achieved an in-plane displacement, but it was only 1.4 microns with 200 V [39]. Another design that studied the extension of travel range of comb drive actuators using tilted folded beam achieved in plane displacement of about 61µm at actuation voltage of 45 V [40].

One of the works that enabled large in plane stroke was that of Dr. K. Pister et at. based on electrostatic inchworm motor. The first electrostatic linear inchworm motor design achieved high displacement of 80 µm and force of 260 µN at 33V. The force density of this design was 87 µN/mm^2. [41]. This design was later optimized to get the force density of around 2 mN/mm^2 for operation at 100 V. The maximum forces reported by electrostatic inchworm motors are under 2 mN. The maximum observed in-plane displacement was 124 µm [42]. The inchworm motor is designed to have two x-y actuators and one sliding shuttle. The x-y actuator has a pawl that is connected to sets of actuator arrays which are orthogonal. For moving the shuttle, the pawl gets engaged to the shuttle by using the clutch-GCA array. This then pushes or pulls the shuttle using the drive-GCA array. During this inchworm cycle, two x-y actuators causes the alternate motion of the shuttle for accumulating large displacements incrementally. Hence, this technique decouples the actuator force from maximum displacement. The design was later optimized in a later study which also uses in-plane electrostatic gap-closing actuators along with a flexible driving arm mechanism to improve motor force density. In this optimized work, the motor operates similarly to other inchworm-based microactuators by accumulating small displacements from the actuators into much larger displacements in the motor. A full motor design optimization was performed to maximize motor force density by using an analytical model of the inchworm motor based on the static force equilibrium condition. Alongside this, for calculating the theoretical motor efficiency for different motor designs, force losses from supporting flexures were included. The force density optimization analysis of the gap-closing actuators and supporting motor structures was done which gave basis for the design and manufacture of the inchworm motors with flexible driving arms and gap-closing actuators. In this optimized design, the in-plane inchworm motor introduced that implements an angled flexible drive arm which allows both grabbing and pulling the shuttle with one actuator. The design of the gap-closing actuators is symmetric on each side. This allows the shuttle to balance out the reactions from the engaged drive arms and also enables moving even untethered shuttles. Hence only the length of the shuttle limits the displacement. The motor required only a single-mask fabrication and demonstrated robust performance, a maximum speed of 4.8 mm/s, and a maximum force on the shuttle of 1.88 mN at 110 V which corresponds to area force density of 1.38 mN/mm^2. Maximum displacement of a parallel plate actuator is limited mainly to the pull in effect that happens within the airgap [43].

MEMS actuators that provide out of plane displacement also have great demands in applications such as manipulating in robotics and microrobotics [44], miniature lens positioning for auto focusing/zooming ,micro-positioning stages [45], etc. Such applications require displacement ranges from tens of micrometers to millimeters and actuation forces in the mN range. A number of electrostatic actuator designs with large out of plane displacement have been previously reported. A repulsive force driven large stroke out of plane electrostatic actuator has been reported in [46] reaching out of plane displacement of 86µm for actuation voltage of 200V with overall dimensions of 3mm × 3mm. Another example of a wide range electrostatic actuator is presented in [47] utilizing a curved electrode zipper topology reaching out of plane displacement of 212µm with a 1mm footprint device. The pull in voltage for this device is around 100V and it has a theoretical blocking force of 32 µN.

One of the applications of out of plane stroke actuator is in manipulation of optical components such as microlens. A recent work on this is the design of a novel high performance piezoelectrically driven microlens actuator for micro optics applications that provided large out of plane displacement of 228 µm at 22 V [48]. The footprint area of the entire device is less than 36mm^2 and it has power consumption of 3.5mW. The resonant frequencies of the actuator with and without a micro lens load are 0.89 kHz and 2.1 kHz, respectively. In the design, the micro lens actuator consisted of six individually actuated d31 piezoelectric beams. The beams support a micro lens platform via serpentine springs. The composite actuator structure of the piezoelectric beam is made up of PolySi/SiO2/Ti/Pt/PZT/Ti/Pt thin-film layers. The outer diameter of the micro lens holding platform has is 1500 µm and the inner circular opening of 580 µm to accommodate a lens. When an electric field is applied between the top and bottom electrodes layers, the PZT layer contracts along the x-y plane that produces a moment, which eventually displaces the micro lens holding platform in an upward direction. The performance of this actuator is further enhanced by controlling the residual stress of the structural layers that also did not need any restructuring the design. The actuation performance demonstrated is promising for applications such as hand-held devices, confocal microscopy or pico-projectors where large optical zooming and fast actuation response are essential.

Another microactuator that allowed large out of plane stroke that have a variety of application in optics and micro optics is done by Dr. Ridha Ben-Mrad et al. It is mainly a three-degrees-of-freedom microelectromechanical systems (MEMS) electrostatic actuator that utilizes a piston-tube configuration that enables the use of electrodes with a wide area. This generates a large output force. Alongside that, a flexure mechanism is used in the design in which the stiffness of in plane motion is higher compared to the out of plane stiffness. Such flexure design allows the large translation stroke along Z axis before any lateral pull in happens. The actuator that had been designed and fabricated was able to give a pure translation (piston style motion) of) of 28 µm at 80 V and an angle of rotation of 0.78° at 70 V. A mass of 1 mg was translated 24 µm at 80 V, This indicate ability of the actuator to provide high output force. The actuator was fabricated using the Micralyne Micra GEM-Si MEMS fabrication process, in which the pistons and tubes are fabricated in the device layers of two bonded Silicon on insulator (SOI) wafers. There is two parts to the 3-DOF electrostatic piston-tube actuator: one is the moving and other is the fixed parts. The fixed part consists of pistons (teeth) which could have a square, rectangular, circular, or arc shaped cross-sections. The pistons are attached to the base and they form the stator of the actuator. The moving part contains tubes (through holes) that have cross-sections similar to the cross-sections of the pistons. The moving tubes surround the actuator plate, and they are suspended by supporting beams that provide high in-plane stiffness while allowing the rotor to achieve translation along the z-axis. The pistons could be divided into three or more groups that are electrically separated from each other to allow bi-axial rotation of the rotor about the x and y axes. Upon application of voltage across the rotor and all of the stators, an electrostatic force develops between the pistons and the tubes in the z direction. This electrostatic force causes movement of the rotor which is the free upper structure from its static position towards the stators that is fixed lower structure in a pure translation piston-style motion along the z-axis. As the voltage drops, rotor moves back to its equilibrium position due to the restoring mechanical force in the supporting beams. For rotating the rotor of the actuator about the x and/or y axes, voltage is applied across the rotor at only one or two stators. The piston-tube actuator allows use of wide area of the electrodes and can be expanded in two dimensions along the x-y plane to enable large force generation. The force generated by the actuator is directly applied to any load attached to the actuator's central plate without the use of a mechanical amplification mechanism. The actuator also provides 3-DOF motion. The movements are a translation along the z-axis and rotations about the x and y axes. The measured natural frequency of the actuator was 742 Hz, and the measured bandwidth of 1044 Hz. The settling times of the actuator during the actuation and the release states were about 1 ms and 2 ms, respectively. In the rotation mode, the actuator was able to achieve an angle of rotation of 0.78° at 70 V about the x and y axes [49].

Another recent work that was based on small-gap electrostatic micro-actuator presents a design that allows high deflections with small electrode separation [50]. The concept presented makes the huge electrostatic forces within nanometer small electrode separation accessible for large deflections. Electrostatic actuations that are larger than the electrode separation was measured. This was done using a novel electrostatic actuator principle that allows deflection amplitudes which is significantly higher than the electrode separation. By using this actuator concept, high quasi-static as well as high resonant actuation amplitudes are possible at low voltages. The work demonstrated nano electrostatic drive referred as NED actuator geometries for positive and negative cantilever curvatures, and, therefore, for upward and downward actuator deflections. The

NED actuator is composed of periodically repeated electrostatic-force-based elementary actuator cells processed at cantilever surface. A single actuator cell is composed of a base on which two electrodes are placed. They are separated by two spacers on the left and right-hand side of an air gap. The electrostatic potential applied between the top and the bottom electrode is different and that generates an electrostatic force creating a bending of the top electrode, in addition to its downward displacement. The spacers constrain the electrode at the top from large deflection as it gets connected with other parts of the structure, but it produces significant strain in the upper electrode. The top electrode transforms this surface strain to the structure, which then causes to deform the whole actuator and lead to the bending of the associated section of the cantilever. The combination of upward with downward deflectable NED actuators permits bidirectional electrostatic actuation, S-shaped cantilever deformation profiles and thus pure out-of-plane tip deflections. The novel actuator class will benefit from the low-power consumption of electrostatic actuators, the simple fabrication process and the integration with CMOS technologies. It further demonstrates a solution to prevent or reduce the occurrence of pull-in related failure mechanisms of MEMS actuators and sensors.

Inspired by the cellular structure of biological muscles, the large actuator arrays demonstrated in this work bypass this limitation by summing up displacements from hundreds of cascaded actuator cells with submicron individual displacement. Combining large range of motion and scalability along with large force/energy densities paves the way towards the ultimate micromachined actuators that can be adopted for a wide range of applications. Due to the inverse square relationship, the electrostatic force between two parallel plates can be significantly increased by shrinking the air-gap between the plates. Furthermore, small air-gaps in the few microns range and below can withstand much larger electric fields (hundreds of MV/m) compared to the known breakdown field of air for larger scale gaps (3MV/m) .This provides tremendous potential for micromachined electrostatic actuators to realize high energy density with relatively simple structures, materials and fabrication.

CHAPTER 2

ULTRA LOW POWER DIGITALLY OPERATED ACCELEROMETER

2.1 OPERATION PRINCIPLE

Acceleration switches are simple devices with an output that can be high (ON) or low (OFF) depending on the predetermined acceleration threshold of the device and the acceleration the device is subjected to [51]. Most acceleration switches are comprised of a suspended mass anchored to a substrate with flexible tethers. If the device is subjected to an acceleration higher than its threshold value, the suspended mass will come in contact with an electrode, closing a circuit and signaling that the acceleration threshold has been reached. Hence, such devices require close to no power for operation and their output can be directly fed to a digital processor without any further processing. However, an acceleration switch can only indicate whether the applied acceleration is higher or lower than the set threshold and cannot provide quantitative information about how much acceleration is applied to the device at each moment. In other words, an acceleration switch can be referred to as a single bit digital accelerometer. The approach demonstrated in this work is to add digital control ability, via electrostatic tuning, to acceleration switches and turn them into multi-bit digital accelerometers. Therefore, devices shown in this work are acceleration switches that can perform quantitative acceleration measurements with the help of a digital controller.

2.2 DEVICE DISCRIPTION

Figure 2.1 (a) illustrates an 8-bit accelerometer prototype operating based on the principle of an acceleration switch with digitally tunable threshold. It consists of 8 sets of electrostatic actuators mounted around a large proof mass. Each bit of resolution in the sensor response is associated with an electrostatic actuator acting on the proof mass. Once activated, each electrostatic actuator applies an assistive force to the proof mass lowering its switching threshold (by pulling the proof mass towards the output contact electrode). Each actuator applies twice the force to the proof mass compared to the actuator associated with the next less significant bit. For each combination of activated actuators, depending on whether the proof mass contacts the output electrode or not, it can be determined whether the applied acceleration is larger or smaller than the acceleration

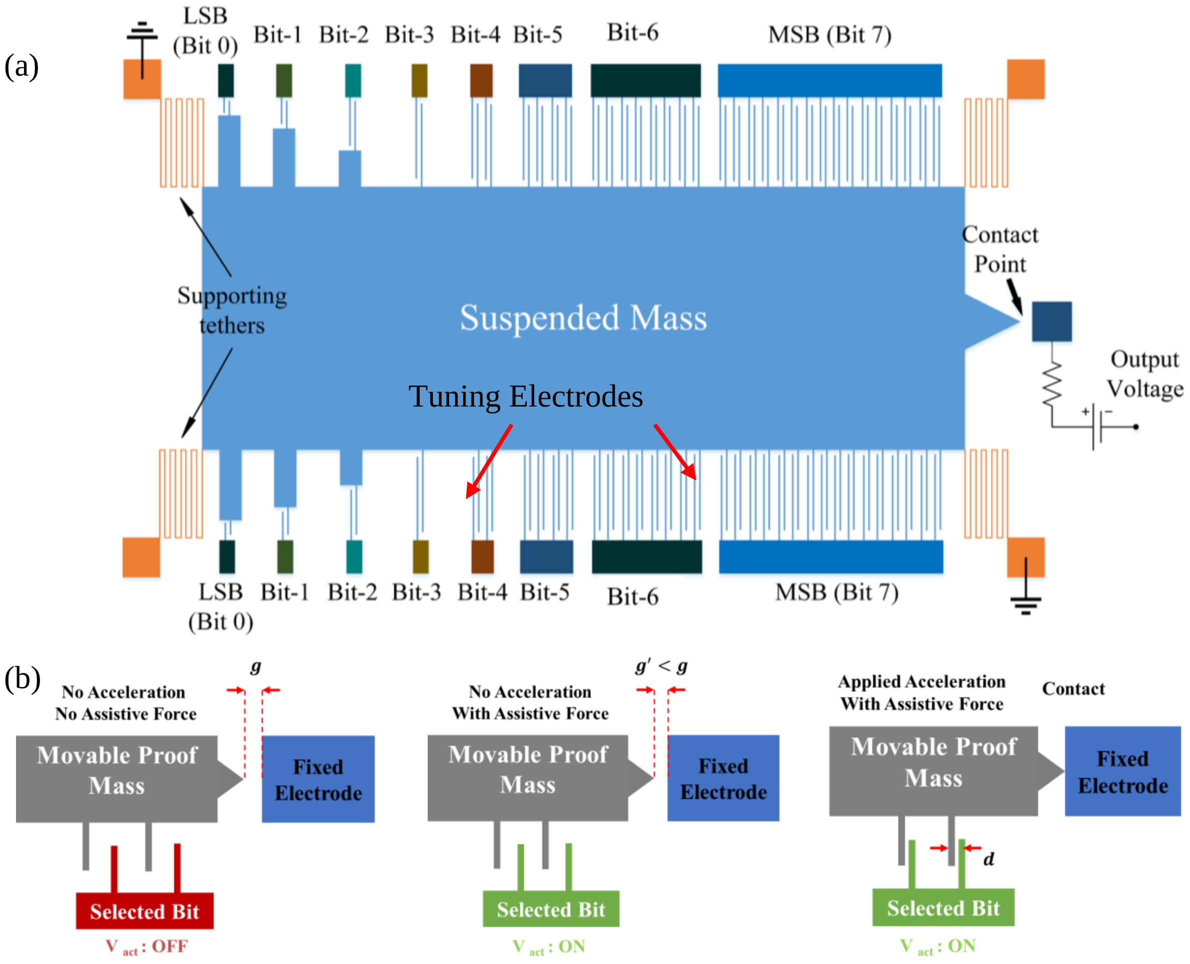

Figure 2.1(a). Simplified schematic of the 8-bit digitally operated accelerometer, (b) Shows simplified schematic of acceleration switch with tuning parallel plate actuator.

threshold for that combination.

The proof mass moves in plane back and forth (for example in the horizontal direction in Figure 2.1.(b)) as a result of the applied acceleration. The proof mass connected to ground (GND) has a metallic tip that comes in contact with a stationary contact electrode when the applied acceleration exceeds the threshold. The stationary output contact electrode is biased with a bias voltage (V_{bias}) through a large resistor. When contact occurs, the output contact electrode voltage will be set to zero. Application of an assistive force which pulls the metallic tip of proof mass towards the output contact electrode will lower the acceleration threshold. In this manner, by having an arrangement of multiple electrostatic actuators with appropriate strengths (appropriate electrode finger size and number) around the proof mass and selectively turning them ON or OFF, binary algorithm can be performed by microprocessor to find the value of the applied acceleration.

2.3 ANALYTICAL MODEL OF DIGITALLY OPERATING ACCELEROMETER

Generally, the analytical model of an accelerometer can be expressed similar to the dynamic model of the mass-spring-damper system. In this way, the dynamic model of an accelerometer can be expressed by:

$$m\,\ddot{x} = b\,\dot{x} + k\,x \qquad (2.1)$$

where m is the effective mass of the sensor, $\ddot{x}$ is the second derivate of the displacement, b is the linear damping, $\dot{x}$ is first derivate of displacement, and k is the overall stiffness of the supporting tethers. On the other hand, for the acceleration switches the static force equation can be expressed at the contact point by:

$$m\,Fsa = k\,x \qquad (2.2)$$

where Fsa is the full scale acceleration which is the acceleration threshold required for contact between stationary electrode and proof mass. Due to the operation principle of the tunable acceleration explained in section 2.2 the acceleration threshold of the acceleration switches can be tuned by applying the electrostatic assistive force using parallel-plate electrostatic actuators. The parallel-plate electrostatic force is given by:

$$F = \frac{n\varepsilon AV^2}{2d^2} \tag{2.3}$$

where the ε is the permittivity of free space (8.854e-12 F/m), n is the number of electrodes, A is the area of electrodes, d is the electrostatic gap size, V is the bias voltage. Based on the description of the device explained in the previous sections, each electrostatic actuator applies twice electrostatic force to the proof mass comparing to the next electrostatic actuator. In this manner, the static force equation at the contact point is expressed by:

$$ma_{applied} + \sum_{n} \frac{2^{(n-1)}\varepsilon AV_n^2}{2d^2} = kx \tag{2.3}$$

where the V_n is the bias voltage which is applied to the electrostatic actuators associated with n^{th} bits of resolution. i.e.

$$V_n = \begin{cases} V_{Bias} & if \text{ the the elctrostatic actuaro of the } n^{th}\ bit\ of\ resolution\ is\ turend\ ON \\ 0 & if \text{ the the elctrostatic actuaro of the } n^{th}\ bit\ of\ resolution\ is\ turend\ off \end{cases} \tag{2.4}$$

2.4 DESIGN CONSIDERATIONS

In order to design the different components of the device, the static force equations of two different cases are to be utilized. In the first case, all the electrostatic actuators have to be turned OFF. Utilizing the equation 2.2, the mass of the proof mass and the stiffness of the tethers needs to be chosen in a way that, the displacement of the proof mass is equal to the contact gap between the proof mass and the stationary electrode, when the full scale acceleration applied to the proof mass.

In the other case, the components of the electrostatic actuators have to be chosen in a way that the electrostatic actuator of the most significant bit applies half of the full scale acceleration to the proof mass. i.e.

$$m.\frac{1}{2}Fsa = \frac{2^7 \epsilon A V^2}{2d^2} \qquad (2.5)$$

In order to avoid the pull-in in parallel plate actuators, the electrostatic gap of the parallel plates has to be chosen 3X larger than the contact gap between the stationary electrode and the proof mass. Also, the actuation voltage needs to be lower than the pull-in voltage of the electrostatic actuator. The pull-in voltage of the parallel plate actuators is given by:

$$V_{pull-in} = \sqrt{\frac{8kd'^3}{27\epsilon A}} \qquad (2.6)$$

where d' is the initial electrostatic gap between parallel plates and k is the stiffness of the supporting tethers.

2.5 DESIGN SPESIFICATION

To perform an acceleration measurement, the tuning electrodes are to be turned ON or OFF in a sequential manner via an interfaced digital controller. Turning an electrostatic actuator ON means application of a pre-determined fixed voltage to that electrostatic actuator by the microprocessor. The actuator associated with the most significant bit (MSB), which is Bit 7 in this case (Figure 2.2), has twice the number of identical parallel plate actuator fingers compared to the next most significant bit (Bit 6). In other words, Bit 7 provides an actuation force which is exactly

$$k.x = \frac{1}{2}m.Fsa + F_{MSB} \tag{2.7}$$

$$k.x = \frac{1}{4}m.Fsa + F_{bit-6} + F_{MSB} \tag{2.8}$$

$$\vdots$$

$$k.x = \frac{1}{256}m.Fsa + F_{LSB} + F_{bit-1} + F_{bit-2} + F_{bit-3} + F_{bit-4} + F_{bit-5} + F_{bit-6} + F_{MSB} \tag{2.9}$$

twice that of Bit 6 when turned on. Similarly, the number of actuator fingers goes down by a factor of two from the most significant bit to the next less significant bit and the least significant bit (LSB) has the minimum number of actuator fingers. In this manner, based on the arrangement of actuated bits of resolution, the static force equation at contact point can be expressed by:

where the F_{MSB}, F_{Bit-6}, F_{Bit-5}, F_{Bit-4}, F_{Bit-3}, F_{Bit-2}, F_{Bit-1}, and F_{LSB} are the assistive electrostatic force associated with electrostatic actuators of each bit of resolution.

However, in order to avoid excessive number of electrodes which in turn increases the size of the device, the area of electrodes of Bit 2, Bit 1 and LSB has been decreased by shortening the length of electrodes by the factor of two. The number of electrodes, electrostatic actuator gap size, and electrode areas are to be chosen so that upon application of the ON voltage to the MSB actuator a force equal to 50% of the full-scale acceleration force is applied to the proof mass. Since, each bit has twice impact comparing to the next less significant bit, an array comprised of the status of all bits indicates an 8-bit binary number which equal to digitalized value of minimum acceleration threshold required for bringing the proof mass to contact with stationary output electrode.

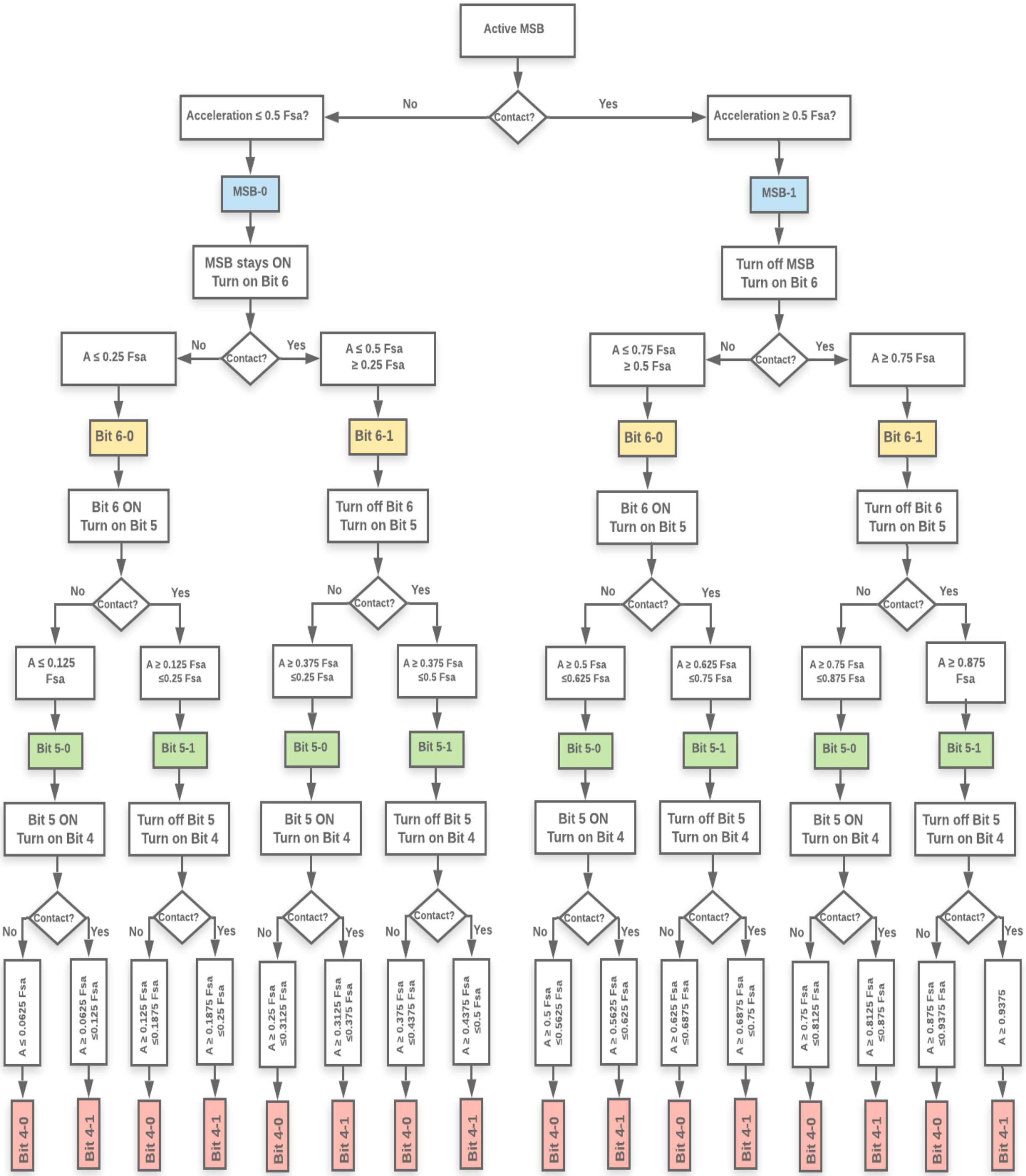

Figure 2.2. Flowchart showing algorithm for binary search for 4 bits of resolution in an 8-bit digital accelerometer.

2.6 BINARY SEARCH ALGORITHM

The binary search to find the acceleration in each measurement cycle starts by activating the MSB electrode. If the switch is closed (electrodes come in contact) due to activation of the MSB electrode only, the acceleration is larger or equal to half the full-scale acceleration. In this case, the first digit (MSB) in the binary output should be “1” (binary output of “1???????”). The MSB electrode will then be turned off and the electrode associated with the next bit is activated. Similarly, if this electrode alone is enough to keep the switch closed, the acceleration is above or equal to 75% of full-scale (and the second digit in the acceleration binary number will be “1” as well, resulted in the binary output of “11??????”). If not, the acceleration is somewhere between 50% and 75% of full-scale (the second digit is “0”, resulted in the binary output of “10??????”). In this case, the 2nd electrode stays ON and the third electrode is activated. If addition of the 3rd electrode closes the switch, the acceleration is between 62.5% and 75% (binary output of “101?????”), otherwise, it is between 50% and 62.5% (binary output of “100?????”). With the same algorithm the other 5 bits can be determined leading to an 8-digit binary output. Therefore, the acceleration amplitude with a resolution of 1/256 of full-scale (8-bit resolution) can be determined through 8 electromechanical operation steps. Figure 2.2 shows the flowchart of the binary search algorithm for the 8-bit digital accelerometer. Due to the size limitation, the flowchart has been provided for only four bits of resolution.

2.7 DEVICE DESCRIPTION AND FABRICATION

Monocrystalline silicon with a thin coating of Ruthenium was used as the structural material for the accelerometers. Figure 2.3 shows the fabrication process used to fabricate the devices on an SOI substrate having a 20 µm thick device layer and 2µm thick buried oxide layer using a two-mask micromachining process. First, a very thin layer (50 nm) of Al_2O_3 has been deposited on the SOI device layer as a hard mask by using the atomic layer deposition (ALD) technique. Then the deposited Al_2O_3 film has been patterned using the first mask (Figure 2.3.(a)). Backside was then patterned and etched to avoid any potential stiction issues for the large proof masses. Then the buried oxide layer under the silicon skeleton has been etched with ICP tool in order to decrease the stress on the (Figure 2.3(b)). The accelerometer silicon skeleton was then defined in the SOI device layer via deep reactive ion etching (DRIE) all the way down to release the device (Figure 2.3(c)). Then the Al_2O_3 has been removed in the hydrofluoric acid (HF 49%). The device has been kept in the HF for 6 minutes to make sure that the buried oxide layer under the wire bonding pads

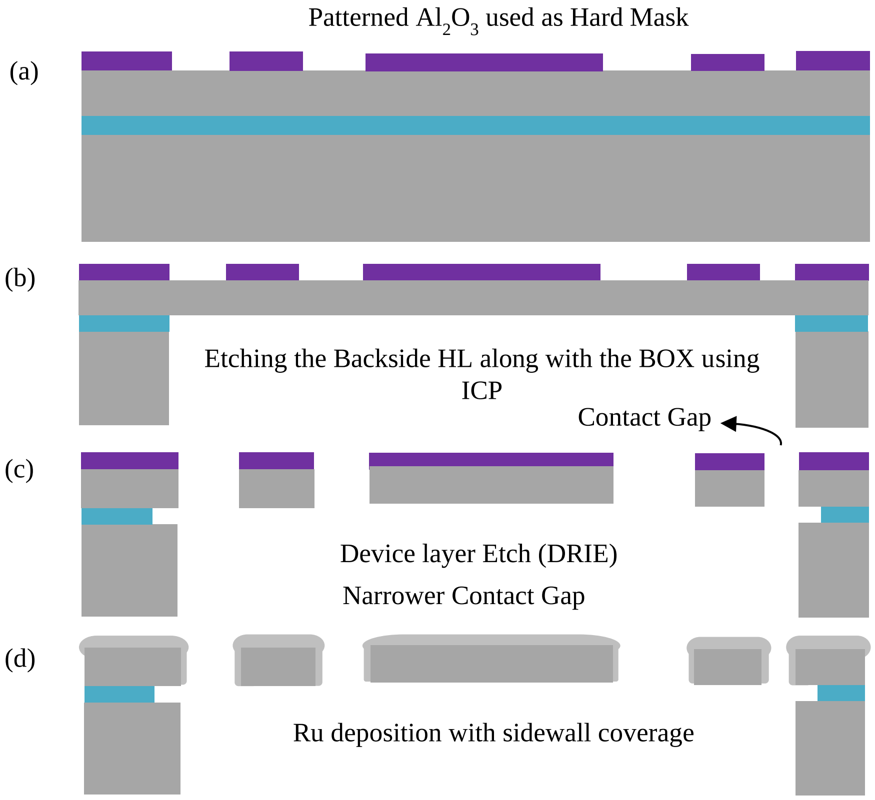

Figure 2.3. Schematic side view showing the microfabrication process flow for the fabrication of the accelerometer.

got over etched. A thin layer of ruthenium (around 400 nm) with slight sidewall coverage was sputtered on the fabricated fully silicon devices to provides a high-quality metal-metal electrical contact between the tip of proof mass and the output electrode (Figure 2.3(d)). Thickness of the deposited ruthenium on the sidewalls was thoroughly monitored to avoid the electrical short circuit between the wire bonding pads.

Figure 2.4 (a) and (b) show SEM views of the digital accelerometer structure fabricated using the described fabrication sequence. Regular lithography and plasma etch constraints restrict the gap size between the proof mass and the metallic tip around 2 µm. (Figure 2.4(b)).

2.8 MEASUREMENT SETUP AND RESULTS

2.8.1 MEASUREMENT SETUP AND RESULTS

The tested 8-bit prototype shown in figure 2.4(a) has a 2.275mm×0.875mm proof mass (104µg), electrostatic actuators mounted around the proof mass shown in figure 2.5(c) has identical electrostatic gap size of the 8 µm, and the length of each parallel plate vary from 400 to 50 µm chosen with respect to the design description and design specification explained in sections 2.3 and 2.4, respectively. The parallel plat four support beams with overall stiffness of 1.4N/m (figure 2.4.(d)), and contact gap of 2µm leading to full-scale acceleration of 2.7g (binary output of 11111111). This relatively big full-scale acceleration would require sophisticated high-g test and characterization equipment that were not available. The MEMS chip was placed on a printed circuit board (PCB) and thus tested for accelerations only less than 1g which could be easily applied by tilting the board at various angles with respect the horizon. It was determined that actuation voltage of 6.7V is to be applied to the actuators associated with MSB, Bit-6, Bit-5, Bit-

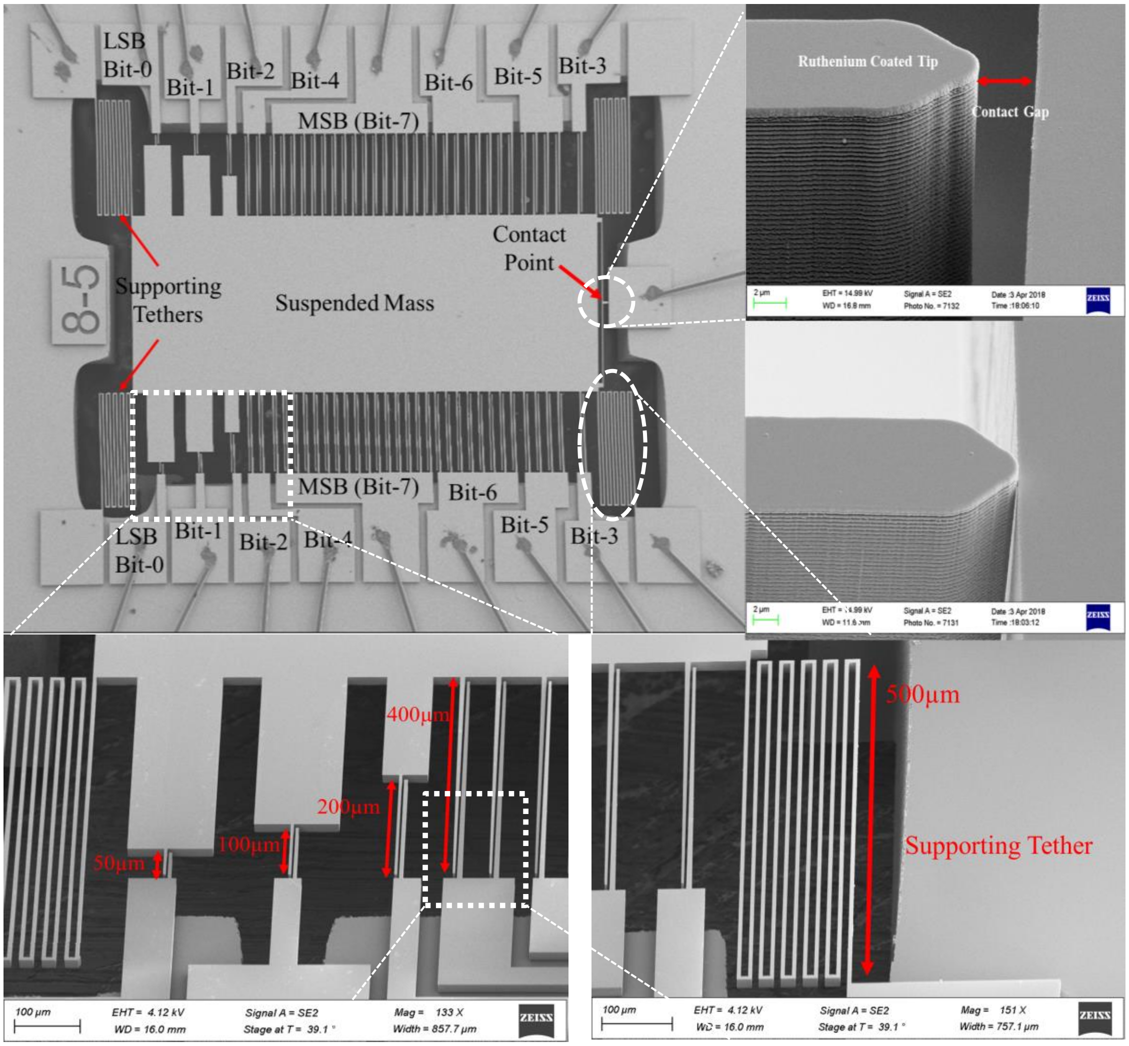

Figure 2.4.(a). SEM view of the fabricated 8-bit digital accelerometer, (b). Shows the zoomed-in views of the output contact tip while the switch is open, (c) Shows the tuning parallel plate actuators acting on proof mass lowering acceleration threshold, (d). Shows the supporting tether to substrate.

4, Bit-3, Bit-2, Bit-1and Bit-0 (LSB) actuators to lower the threshold acceleration by 1/2, 1/4, 1/8, 1/16, 1/32, 1/64, 1/128, 1/256 of full-scale acceleration, respectively. The output resolution of the accelerometer is limited to acceleration threshold of LSB which is10.5mg in this case. Figure 2.5 shows theoretical range of all the 256 possible measured acceleration response of the accelerometer for the applied acceleration. Since the actual output of the designed accelerometer

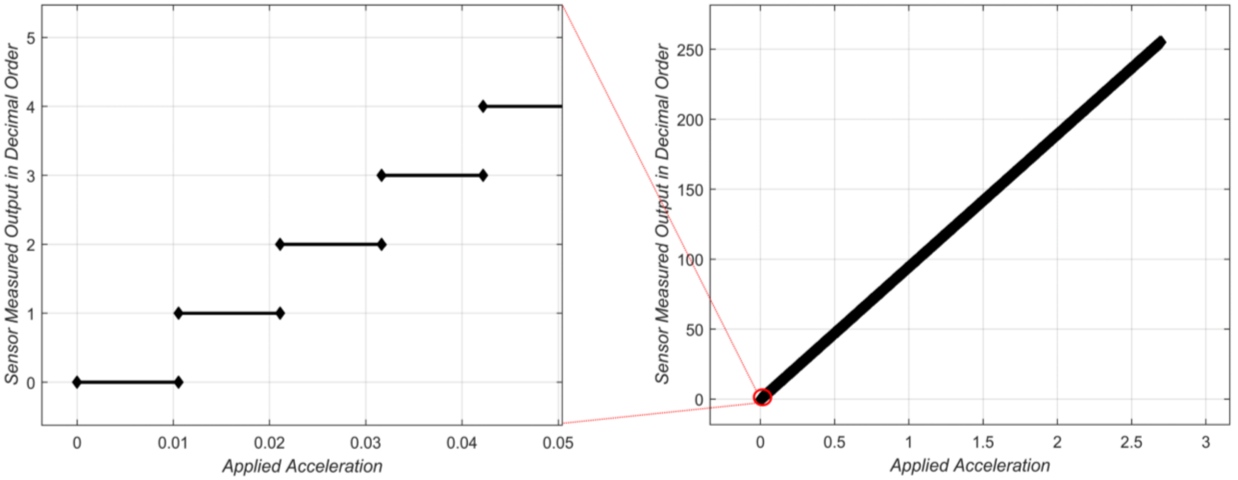

Figure 2.5. The graph shows the measured acceleration in the decimal order vs the applied acceleration the device was subjected along with zoomed-in view of selected points.

is a digital 8-bit binary register, the binary numbers have been converted to the decimal order to graph the measured acceleration vs the applied acceleration for the tested 8-bit accelerometer.

Device performance was validated by applying different accelerations while microcontroller board Arduino Mega2560 was turning the different actuators ON/OFF with running the binary search program. In this manner, each bit of MEMS accelerometer was connected to a digital output pin of the microcontroller through a low power MOSFET transistor. The MOSFET transistor serves as a switch triggered by microcontroller digital output pin (5V) to feed the actuator by the operation actuation voltage which is 6.7V in this case. The stationary output electrode was biased with 3V. The voltage of the output electrode was monitored by the microcontroller in each step of binary search program to indicates if the contact occurs or not.

Table 1 shows resulting sensor binary outputs for different applied accelerations showing the closest possible binary output in each case. Bit values in the Table indicate the ON/OFF (1/0) status of the actuator of the respective bit when contact occurs. Input accelerations are produced

Table 2.1. Measurement results of the 8-bit 2.7g full-scale accelerometer for six selected applied accelerations.

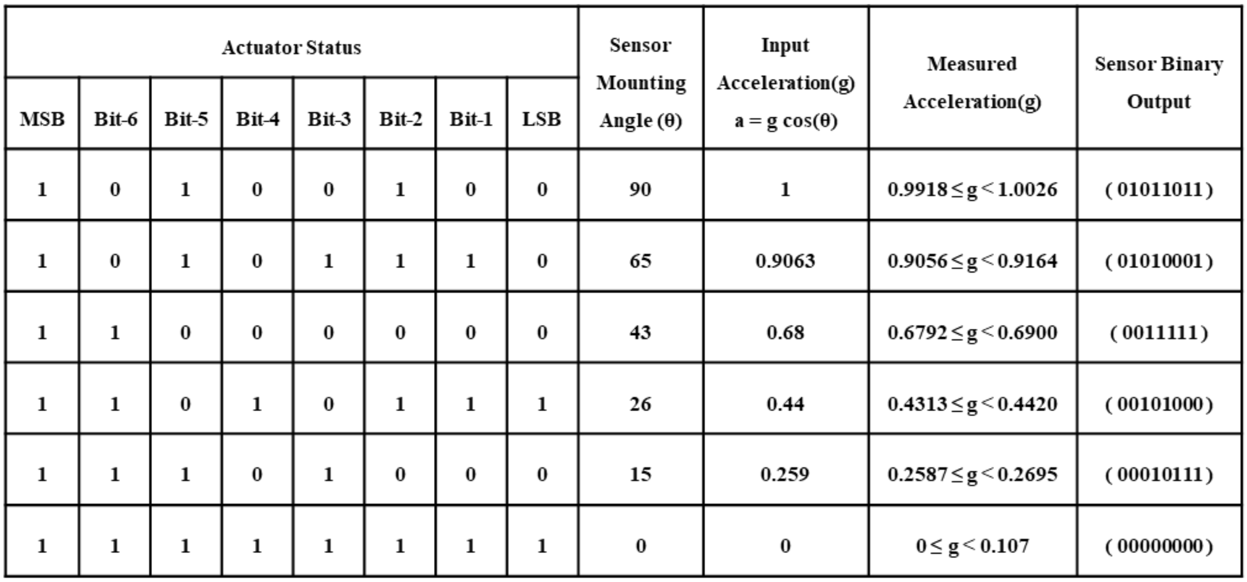

Actuator Status								Sensor Mounting Angle (θ)	Input Acceleration(g) a = g cos(θ)	Measured Acceleration(g)	Sensor Binary Output
MSB	Bit-6	Bit-5	Bit-4	Bit-3	Bit-2	Bit-1	LSB				
1	0	1	0	0	1	0	0	90	1	$0.9918 \leq g < 1.0026$	(01011011)
1	0	1	0	1	1	1	0	65	0.9063	$0.9056 \leq g < 0.9164$	(01010001)
1	1	0	0	0	0	0	0	43	0.68	$0.6792 \leq g < 0.6900$	(0011111)
1	1	0	1	0	1	1	1	26	0.44	$0.4313 \leq g < 0.4420$	(00101000)
1	1	1	0	1	0	0	0	15	0.259	$0.2587 \leq g < 0.2695$	(00010111)
1	1	1	1	1	1	1	1	0	0	$0 \leq g < 0.107$	(00000000)

from the earth gravity (g) by mounting the sensor chip with a certain tilt angle also shown in the table.

2.8.2 TIME AND FREQUENCY RESPONSE

In order to demonstrate the ability of the sensor for real time sensing, frequency and time response of the device were studied. For the given dimension of the fabricated device, the in-plane flexural resonance frequency of 591hz was obtained by:

$$f = \frac{1}{2\pi}\sqrt{\frac{k}{m}} \qquad (2.10)$$

where the k is the stiffness of supporting tethers and m is the mass of proof mass. In order to study the time response of the device, a pulse signal with different frequency and amplitude applied to the MSB while the voltage of the output electrodes was monitored. Since the electrostatic force

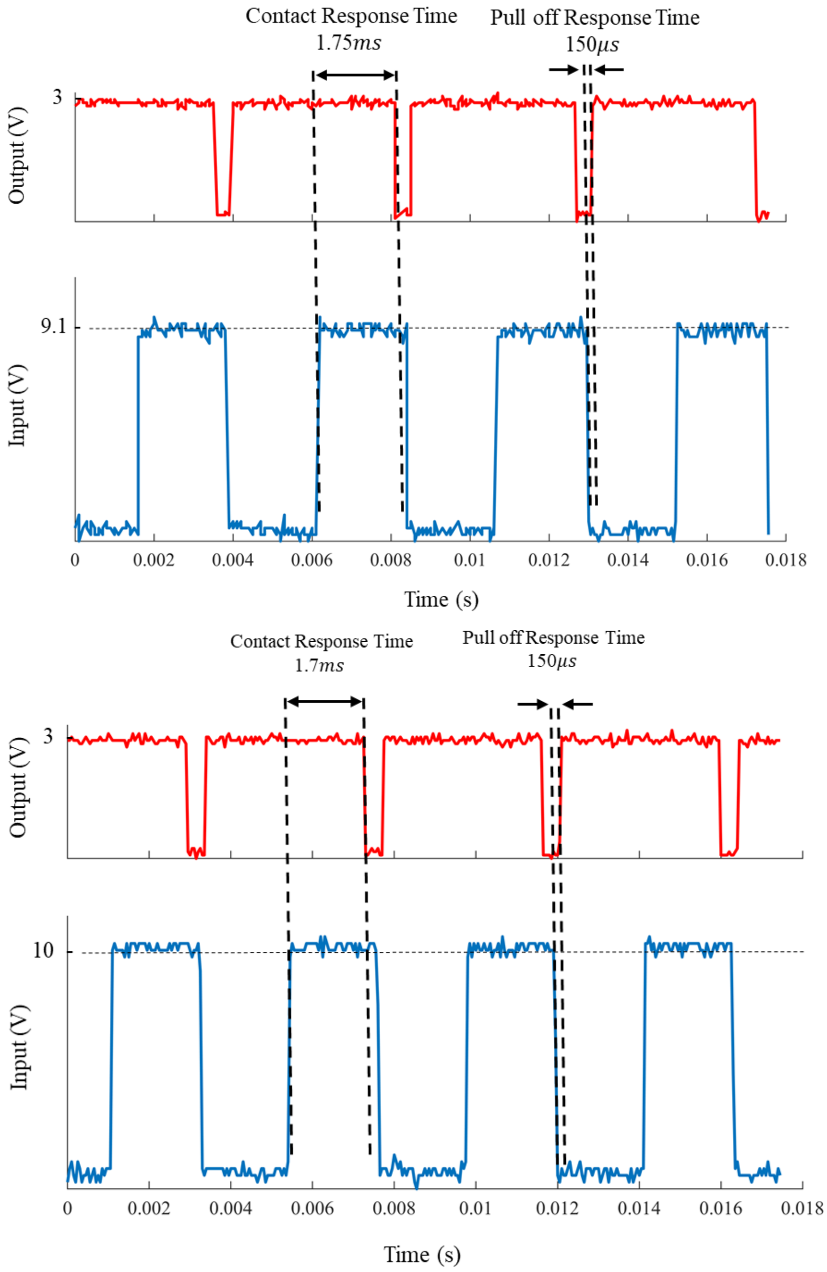

Figure 2.6.(a). Time response of the device to a pulse signal with frequency of 260hz and amplitudes of 9.1V_{pp} applied to the MSB, (b). Showing the Time response of the device to a pulse signal with frequency of 260hz and amplitudes of 10V_{pp}.

applied to the device is relative to square of the actuation voltage, the frequency of the input signal has been set to half of the resonance frequency of the device. In this case, we have observed that the device only responses to the actuation signal with the frequency up to 260hz. The time response of the device was obtained from the difference between the rising time of the input signal (actuating the device) and the falling time of the output signal (closing the switch). In this manner, time response of 1.75ms obtained for amplitude of 9.1V_{PP} and frequency of 260hz (Figure 2.7.(a)). This input signal applies acceleration close to Fsa to the device. It has been observed that by increasing the amplitude of the input pulse signal to 10VPP, the rising time response of the device has been decreased to 1.7ms (Figure 2.7.(b)). Also, the retrieving time response of 150µs was obtained from the difference between the falling time of the input signal and the response time of the output signal. The retrieving delay of the device is mostly resulted from the stiction force between tip of the proof mass and the output electrode.

2.8.3 RELIABILITY

One of the main issues in any type of MEMS contact switches is stiction force which refers to unintentional surface adhesion between stationary electrode and moving electrode at contact point when the restoring force was unable to retrieve the moving electrode from the contact point. There are number of the small forces which are responsible for most stiction forces in MEMS devices: capillary attraction, electrostatic force, hydrogen bonding, and van der Waals force [52]. Regarding to the operation principle of the multi-bit digitally operating accelerometer, stiction force between tip of the proof mass and contact electrodes can result in the failure of device operation. In this case, stiction force results in a hysteresis between required actuation force and restoring force required to retrieve the device from contact point. In order to approximate the stiction force between tip of the contact electrode and the output electrode, hysteresis behavior of the device shown in figure 2.8 was studied with manually tuning the restoring force.

In this manner, all tuning electrostatic actuators were biased with a DC voltage of 6.7V to bring

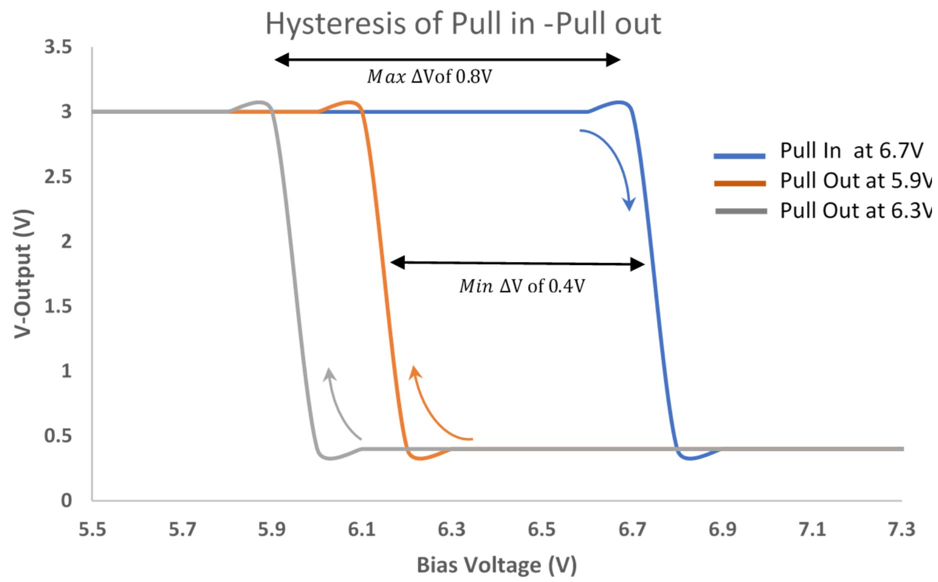

Figure 2.7. The hysteresis graph for output voltage while the actuation voltage required for contact was lowered in order to retrieve the tip from contact point

the proof mass to contact with the output electrode while the voltage of the output electrode was monitored. Then the actuation voltage was gently lowered till the proof retrieve from the contact point. The stiction force of 0.63μN obtained from the difference between the actuating electrostatic force required for contact and the lowered electrostatic force at peeled off point.

$$stiction\ force = \frac{\epsilon A V_{contact}^2}{2d^2} - \frac{\epsilon A V_{no\ contact}^2}{2d^2} \qquad (2.11)$$

Furthermore, reliability of the device was characterized based on the number of the contacts before the failure of the device. In order to perform the reliability test, the ohmic resistivity between metallic tip of the proof mass and the output electrode (coated with ruthenium thin film) has been monitored for a long-time operation of the device. In this manner, electrostatic actuator of MSB was fed by pulse signal with predetermined frequency of 50hz and amplitude of $9.1V_{PP}$, while the output electrode was biased with a DC voltage of 3V through a very large resistivity of 100kΩ.

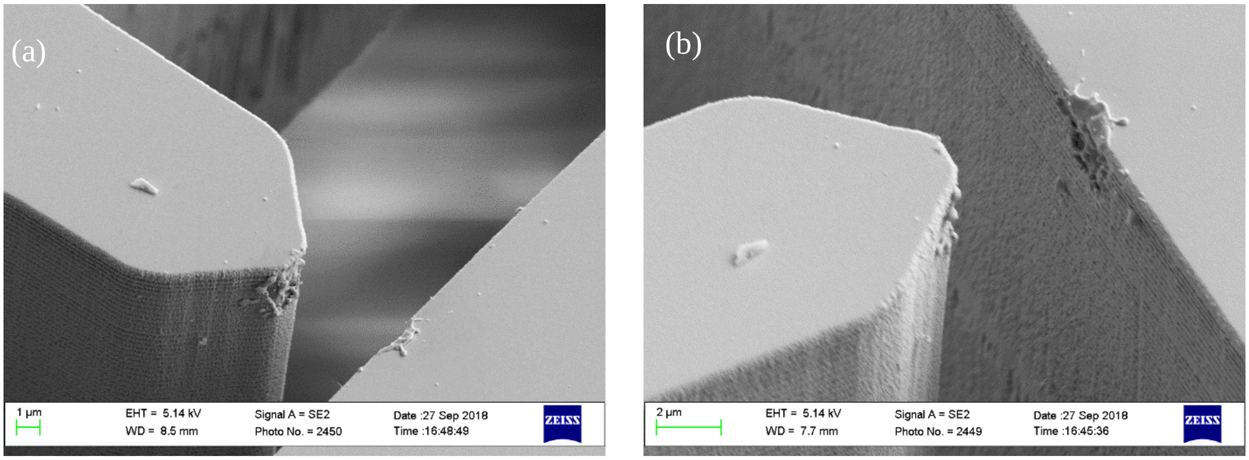

Figure 2.8.(a). SEM view of the contact tip after the long-term operation causing damage to the metal film. (b), SEM view of the damaged metal film on output electrode.

Similar to electrical configuration of the device during the acceleration measurement operation, proof mass was electrically grounded. Contact between the tip of the proof mass and output electrode closes the electrical circuit and results in a DC current through the contact point. In this manner, the ohmic resistivity of metal- metal contact has been simply achieved by the ohm's law. The ohmic resistivity of 1.2kΩ has been measured for the very early cycles of operation. Damage of the thin film metal deposited on the silicon skeleton increases the ohmic resistivity of the contact. The ohmic resistivity of around 1MΩ has been measured after the damage of the metal film. Figure 2.7 shows SEM zoomed-in view of the both sides of the contact point after 17.5 million cycles of operation.

2.8.4 OPERATION POWER CONSUMPTION

The digitally operating accelerometer is just a passive switch operating based on the acceleration it is subjected to. In addition to the power consumed by the MEMS sensor, the digital processor responsible for turning “ON” and “OFF” the electrodes will require some power for its operation as well. During each measurement cycle, each actuator or electrode needs to be turned “ON” once. The overall electrode capacitance of the tuning electrodes in the device is calculated to be 0.56pF. Assuming a conservative scenario where each electrode has 0.5pF of parasitic capacitance along with it, the total capacitance to be charged up to the system operating voltage and eventually depleted during each measurement cycle is 39pF. With an operating voltage of 66.7V, the required energy for each measurement cycle would only be 879pJ. For taking 100 measurements per second, i.e., a sampling rate of 100Hz, the consumed energy for operation of the sensor will be 87.9nW of power consumption only, which is considerably lower than the power consumption of a regular Analog front end for MEMS accelerometers.

2.9 SUMMERY AND FUTURE WORKS

It was demonstrated that the concept of contact-based acceleration switches can be enhanced to perform higher resolution quantitative acceleration measurements. A digitally operated MEMS accelerometer with 8-bit of resolution was successfully demonstrated. A simple 2-mask fabrication process was used to fabricate the devices and the contact gap size was reduced by a simple mask less fabrication technique. Also, it has been demonstrated that by performing a binary search utilizing digital microcontroller, the applied acceleration can be determined. The tested 8-bit prototype shows good agreement between the applied acceleration and sensor output with resolution limited by the number of bits, i.e. 1/256 of the full-scale acceleration (10 mg for full-scale acceleration of 2.7g). Elimination of the need for the analog front-end and analog signal conditioning can lead to significant power savings and a leap forward towards ultra-low power MEMS inertial sensors. The same operation principle can be utilized to implement for for 3-axis accelerometer and other type of motional sensors.

CHAPTER 3

ARRAYED CELLULAR ELECTROSTATIC ACTUATOR

3.1 MOTIVATION AND BACKGROUND

Electrostatic forces are what hold our physical world together at the atomic and sub-atomic level and are therefore fundamentally very strong. At macroscale, however, due to strong dependence on the distance (gap size) between involved electrical charges, electrostatic forces tend to be too small for most applications. Furthermore, relatively low breakdown fields (3 MV/m) for macroscale airgaps does not allow accumulation of large amounts of electrical charges on

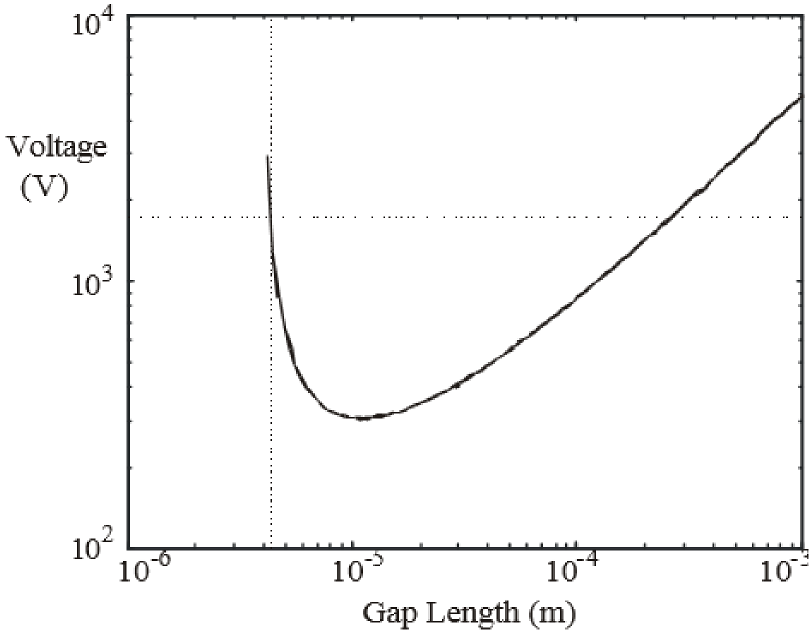

Figure 3.1. Breakdown voltage for air gaps with different sizes given by Panchen's law [53]. While a linear trend exists for larger gaps in the millimeter range (constant breakdown field), the breakdown fields are significantly higher for microscale gaps.

electrodes for force generation. With breakdown field of 3 MV/m, the maximum achievable energy density for macroscale air-gaps (100µm and above) is only around 40 µJ/cm^3. Although known to be relatively weak compared to piezoelectric and thermal actuators, electrostatic actuators are commonly used in MEMS and Microsystems providing moderate levels of force. This is mainly due to the fact that narrow air-gaps with sizes in the few microns range can withstand much higher electric fields without breakdown. For example, application of 20-100V across 1-2µm capacitive gaps is quite common for both parallel-plate and comb-drive MEMS actuators (fields up to 100 MV/m).

This trend is explained and demonstrated by Panchen's Law (Figure 3.1.) [54], certifying that while breakdown voltage of air for larger gaps is a linear a function of the gap size (constant breakdown field of ~3 MV/m), for microscale gaps of 100µm and below, the breakdown field increases significantly. The breakdown field especially increases dramatically for air-gaps smaller than ~5µm. This can be simply explained by the fact that within a narrow gap, there is not enough distance for charged particles to accelerate and gain adequate kinetic energy to ionize gas molecules and start the avalanche breakdown.

It should be noted that Panchen's law only predicts the possibility of avalanche breakdown of gases within the gaps (Townsend avalanche mechanisms for gas ionization), and does not consider other phenomena such as field emission and electron tunneling that are common in narrower (especially submicron) gaps [55]. Nonetheless, electric fields required for field emission are in the order of 1 GV/m and field emission can only occur between conductive surfaces. Tunneling, on the other hand, only occurs in nanoscale gaps and addition of a dielectric layer to the surface highly suppresses the possibility of electron tunneling. We have not been able to identify a comprehensive study determining breakdown limits for submicron airgaps between electrodes covered with insulating thin films. However, a breakdown voltage of 3.8 V (via tunneling) has been measured in [56] for a 4nm airgap between metallic electrodes covered by a 4 nm thick layer of insulating carbon (referred to as diamond-like carbon). Despite the fact that tunneling generally has an exponential behavior with respect to gap size, if we assume a conservative linear dependence, the breakdown voltage for a 100 nm gap, based on this reported data, should be around 95 V. which is above the required voltages for the arrayed cell actuator to reach the desired energy density goal. Furthermore, dielectric layers covering the electrode sidewalls in the design is in the 300-800nm range, much thicker than the 4nm carbon layer used in the abovementioned experiment. This works takes advantage of the unmatched capabilities offered by the HARPSS process to realize ultra-narrow high aspect ratio electrostatic actuation gaps to achieve high energy densities at relatively low actuation voltages (below 200 V, possibly below 20V).

The arrayed cellular electrostatic actuator is based on the structural arrangement of individual microscale electrostatic actuator cells with submicron transduction airgaps in large 2-dimensional suspended arrays. The arrayed cell structures are inspired by the cellular structure of biological muscle tissue. Individual animal muscle cells have very limited deformation and force output. However, millions of such cells forming a tissue can provide significant displacement and force by adding the force and displacement of individual cells. Displacement range of the movable electrode in a parallel plate electrostatic actuator is limited to the airgap between the electrodes. Therefore, a tradeoff exists between the achievable energy density and operating voltage of such actuators, and the range of displacement, which is limited to the distance (airgap) between the parallel plates. So, the arrayed cell structures can bypass this limitation and allow realization of electrostatic actuators with both high energy density (small airgaps) and large displacements.

3.2 DEVICE DESCRIPTION AND OPERATION PRINCIPLE

3.2.1 DEVICE DESCRIPTION

Figure 3.2 shows the schematic view of the suspended array of silicon mesh structure. The frame (backbone) of the suspended actuator array is a crystalline silicon mesh with moderate stiffness and ability to undergo strains of around 10 %. Each actuator array unit consists of a large number of electrostatic parallel-plate actuator cells lined up in two dimensional arrays. The force

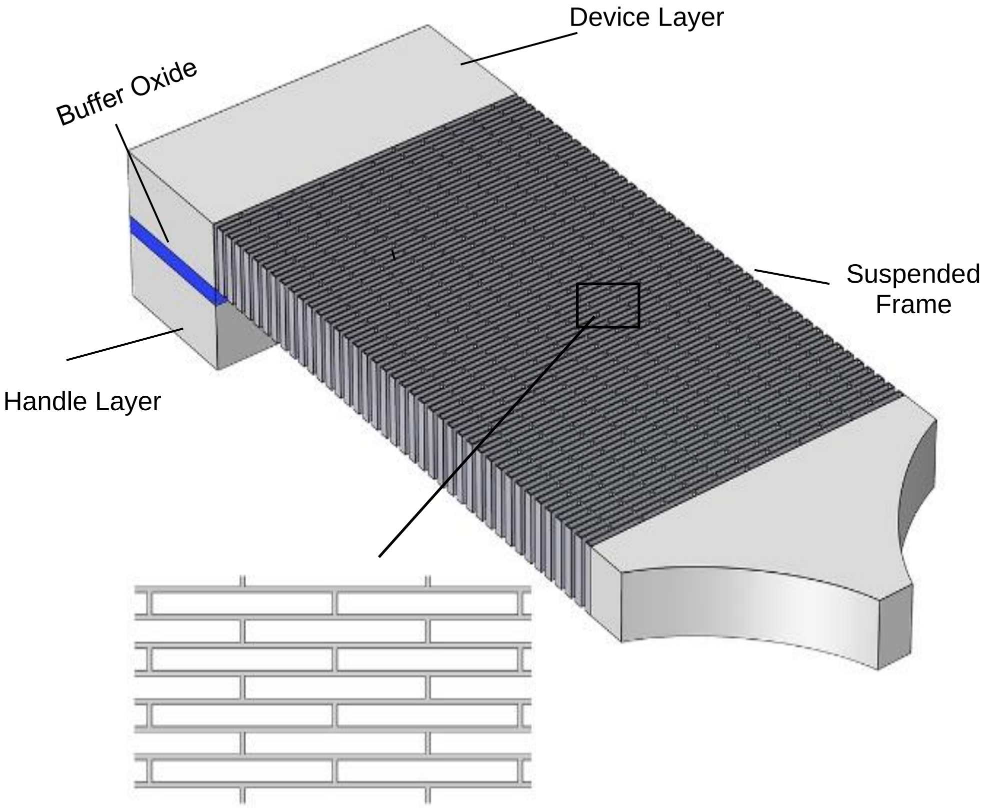

Figure 3.2. Schematic diagrams showing a silicon mesh with brick wall structure forming the main frame (backbone) of an arrayed cell actuator

and displacement of individual microscale actuator cells within the array are added up leading to large actuation forces and large deformation (displacement) range.

The openings within the mesh are filled by a network of polysilicon electrodes separated from the silicon walls by actuation gaps of 250 nm. Two submicron capacitive airgaps are formed within each cell between the silicon frame and the trench refilling polysilicon electrode (Figure 3.3.(a)). The silicon mesh can shrink significantly in the actuation direction while maintaining relatively low stress levels. Sidewalls of the silicon mesh are covered by a thin dielectric film of low stress silicon nitride that serves multiple purposes (Figure 3.3.(b)). The cellular suspended mesh structures offer mechanical flexibility and large deformation achievable in soft materials. The

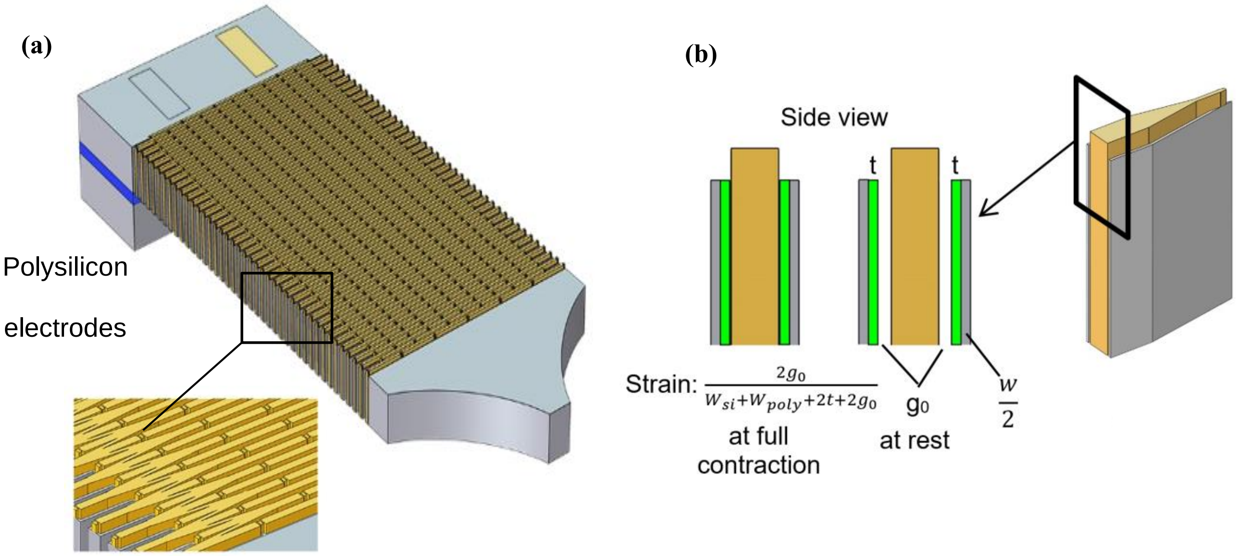

Figure 3.3.(a). Silicon frame with polysilicon electrodes filling the openings within the mesh and separated from the sidewalls by ultra-narrow capacitive transduction gaps; (b). Cross-sectional view of a single cell showing maximum possible strain upon complete closure of the two airgaps.

mesh structure also provides excellent design flexibility, scaling ability, and meta-material-like properties potentially leading to interesting properties.

Sidewalls of the silicon mesh are covered by a thin dielectric film (500 nm low stress silicon nitride, Si_xN_y) that serves multiple purposes. The dielectric film prohibits short circuits between the electrodes biased at high voltages upon contact. It also increases the air-gap breakdown field significantly by blocking flow of electrons due to field emission or tunneling. The thin dielectric film also helps with linearization (pull-in suppression) of the parallel plate electrostatic actuators while increasing the maximum actuator force (due to its relative permittivity > 1). Alongside this, silicon nitride is also known to suppress stiction and can therefore reduce the possibility of the electrode surfaces sticking to each other upon contact.

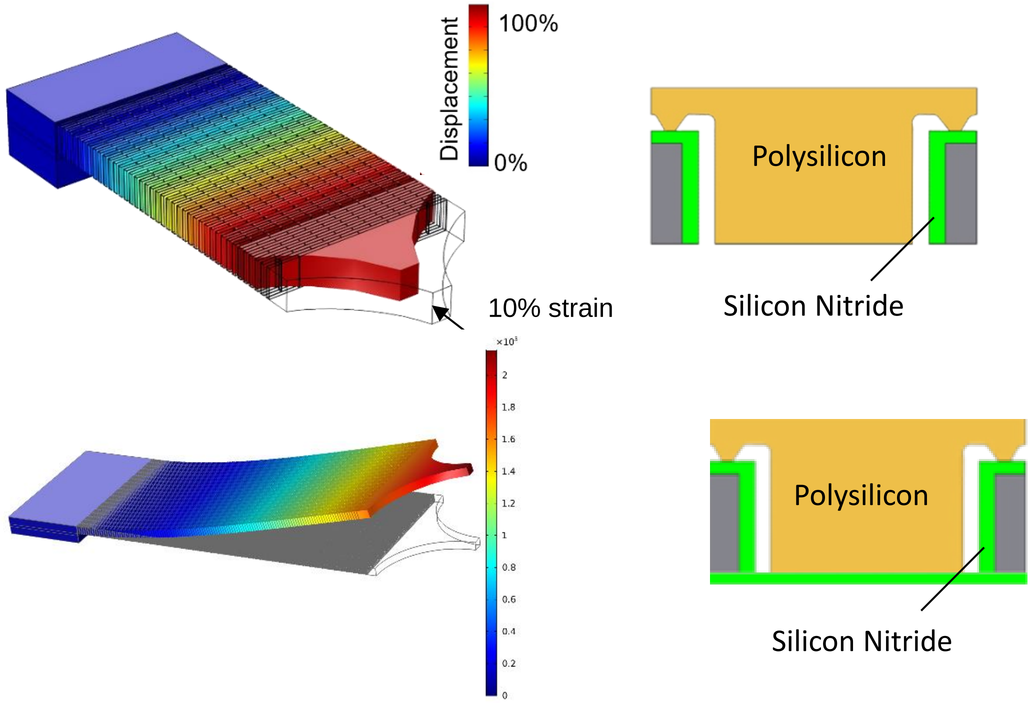

Figure 3.4.(a). Displacement profile of the silicon mesh under compressive axial strain of 10% along with cross sectional view of one cell, (b) Displacement profile of the silicon mesh curved due to the applied bending moment.

Upon application of the actuation voltage between the polysilicon electrodes and the silicon frame, the lateral electrostatic forces pull the silicon mesh sidewalls towards the electrodes leading to overall contraction of the whole frame (Figure 3.4.(a)). Each polysilicon electrode is to be laterally anchored onto the silicon mesh at nodal locations (locations with close to zero deformation) to have adequate stiffness to pull the silicon walls towards itself without getting deformed or pulled in. The interconnects between different polysilicon electrodes are flexible so that the whole polysilicon electrode network also contracts along with the silicon mesh. Displacements in the hundreds of microns range can be achieved for the arrayed actuators without the need for additional flexures to increase the displacement.

Furthermore, one of the challenges of implementation of micro-actuators in most of the applications such as OIS/AF manipulators is the ability of the actuator in moving in both horizontal and vertical directions. While an arrayed cellular electrostatic actuator is mainly suited for horizontal (in plate) contraction, in current lab prototypes vertical (out of plane) displacement has been demonstrated by keeping a silicon nitride thin film (deposited as a necessary part of the fabrication process) on the bottom surface of the actuators. The residual thin film kept on the actuator bottom-side leads to an overall bending moment bending the actuator upwards as shown in figure 3.4.(b).[57].

So, to sum up, the main objective of the designed actuators are as follows:

1. Using ultra-narrow insulated air-gaps, capable of withstanding giant electric fields, as the actuator “material” to achieve the desired high energy densities at relatively low operating voltages. Air does not have defects, does not require deposition process development and characterization, and can withstand very large electric fields within submicron gaps.

2. Utilizing the HARPSS fabrication technique and its extended multi-poly version as a viable approach to implement the narrow air-gaps.
3. The cellular suspended mesh structures offers mechanical flexibility and large deformation achievable in soft materials. The mesh structure also provides excellent design flexibility, scaling ability, and meta-material-like properties potentially leading to interesting properties.
4. Fully silicon micro-machined structures facilitate integration within batch fabricated micro-machined platforms.

3.2.2 ACTUATOR FORCE CALCULATION

Parallel plate actuator configuration is chosen since it can produce larger forces per actuator volume compared to comb-drives. The inverse square dependence of the electrostatic force between parallel plates ($F_{elec,pp} = \frac{\varepsilon_0 A V_{act}^2}{2g^2}$) especially makes parallel plates an attractive option for actuators with small capacitive gaps targeted here. It is also much less challenging to fabricate parallel plate actuator cells using the HARPSS process (no need to etch polysilicon inside deep trenches). On the other hand, parallel plate actuators have relatively small range of motion limited by their air-gap size. In case of the parallel plate cells, as mentioned earlier the maximum achievable deformation of individual cells is equal to the sum of the two air-gaps, i.e. $2g_0$. The resulting strain will be the ratio of $2g_0$ to the total cell width, which includes the widths of the silicon frame, polysilicon electrode, airgaps, and the sidewall dielectric films (Figure 3.3.(b)). Only half of the silicon frame width on each side of the cell should be considered in the total width calculation as the cells share the sidewalls and the outer half of the sidewall should be considered part of the adjacent cell. Assuming silicon frame and polysilicon electrode width of 1μm each, and the airgap and dielectric thickness both being 200 nm, the total cell width would be 2.8 µm. With total cell deformation of 400 nm (sum of the two air-gaps), cell and therefore arrayed cellular electrostatic actuators maximum strain would be 10%.

Force equation for parallel plate actuators with dielectric covered sidewalls is given by

$$F_{elec,pp} = \frac{\varepsilon_0 A V_{act}^2}{2(g+\frac{t_{di}}{\varepsilon_r})^2} \qquad (3.1)$$

where ε_0 is the permittivity of air (8.85×10^{-12} F/m), A is the electrode area, V_{act} is the actuation voltage, g is the air-gap width, and t_{di} and ε_r are the dielectric thickness and relative permittivity respectively.

When dielectric films cover both electrodes across the air-gap, t_{di} represents the sum of the thickness of both films. With a 200 nm thick silicon nitride film as the dielectric ($\varepsilon_r = 8$), and air-gap of 200 nm, such actuator can generate maximum normal stress of up to $\sigma_{n,max} = 7.08V_{act}^2$ kPa (when the air-gap is about to close and electrode dielectrics are about to touch), and minimum normal stress of $\sigma_{n,min} = 0.087V_{act}^2$ kPa (when the actuator is at rest with air-gap at its maximum, g_0).

3.2.3 MAXIMUM OPERATING VOLTAGE

Given the large breakdown fields for ultra-narrow airgaps between dielectric covered electrodes, it is expected that the maximum operating voltage of the proposed devices will be limited by breakdown of the dielectric film. The electric field in the dielectric will reach its maximum when the electrodes come in contact (maximum strain). Different values have been reported in the literature for breakdown field of LPCVD silicon nitride ranging between 7.0 and 12.3 MV/cm [58]. As a conservative estimate, we limit the actuation voltage to 90% of the lower reported breakdown field of 7.0 MV/cm, i.e. 6.3 MV/cm. Consequently, for the 200 nm nitride thickness in this example, maximum operating voltage would be 126V resulting in maximum normal stress of ~112 MPa in the actuation direction, when the airgap is about to close. This is equivalent to 11,200 N of actuation force per 1 cm^2 of actuator surface, or 22.4 N for a 50 µm thick, 4 mm wide actuator. The minimum force, before the actuator has started contracting, i.e. when the actuator gap is at its maximum (g_0), in this example, would be 138 N/cm^2, i.e. 0.276 N for a 50 µm thick, 4 mm wide actuator.

The 81X difference between the maximum and minimum force (depending on where the actuator is within its range of contraction) shows high nonlinearity of the actuator behavior, which is expected for parallel plate actuators. The maximum to minimum force ratio can be significantly reduced by increasing the thickness of the dielectric film compared to the airgap.

3.2.4 ENERGY DENSITY CALCULATION

Given the highly non-linear behavior of voltage controlled parallel plate actuators, to find the actuator energy density, it would be preferable to use the energy method. The mechanical work performed by the actuator, if it is allowed to contract all the way (air-gaps closing), would be the difference between the electrical energy stored in the cell capacitor in its fully contracted form, and its initial at rest position (before any displacement), i.e.

$$E = \frac{(C_{max} - C_{rest})V_{act}^2}{2} \qquad (3.2)$$

where C_{max} is the total array capacitance in its fully contracted position and C_{rest} is the total array capacitance at rest.

For instance, C_{rest} considering both air-gap and nitride film is 28.1 µF/cm^3 (silicon and polysilicon volumes are included in capacitance density calculation), and C_{max} is estimated to be 253 µF/cm^3, leading to overall energy density of 1.78 J/cm^3 (for 126 V actuation voltage). Therefore, the actuation voltage required to meet the 1 J/cm^3 target for this set of design parameters is 95 V.

For the sake of comparison, commercially available bulk PZT actuators offer maximum strain of ~1 µm/mm (0.1%), and blocking stress of slightly above 20 MPa, leading to energy density of ~10 mJ/cm^3, with similar actuation voltages. Based on the analytical results of the above, design parameters are adjusted considering the fabrication limitations also.

3.2.5 ACTUATOR OPTIMIZATION FOR LOWER OPERATING VOLTAGES

Operating voltage is an important parameter for the proposed actuators. Lower operating voltage not only simplifies the supporting electronics, but also improves reliability of the devices (lower chance of dielectric breakdown or discharge). Therefore, a Figure of Merit for the arrayed actuators that will be considered as the user defined metric, is the actuation voltage required to reach 1 J/cm^3 of energy density.

Given the large number of parameters involved it is imperative to have some insight into the effect of each of the parameters on the device characteristics. Graphs in Figure 3.5 show the abovementioned figure of merit (actuation voltage needed for 1 J/cm^3 energy density) as a function of different design parameters and compares the required voltage with the maximum voltage limit set by nitride film breakdown (based on 6.3 MV/cm maximum field assumption). Figure 3.6 shows the required operating voltage as a function of the air-gap size for different silicon nitride thicknesses assuming minimum feature size of 1 µm for defining the artificial muscle structure.

From the graph in Fig 3.5, it is clear that increased dielectric film thickness increases the required actuation voltage, however, for a specific dielectric thickness, lowering the air-gaps below a certain limit (around one fifth of the dielectric thickness) decreases the achievable energy density for the same actuation voltage.

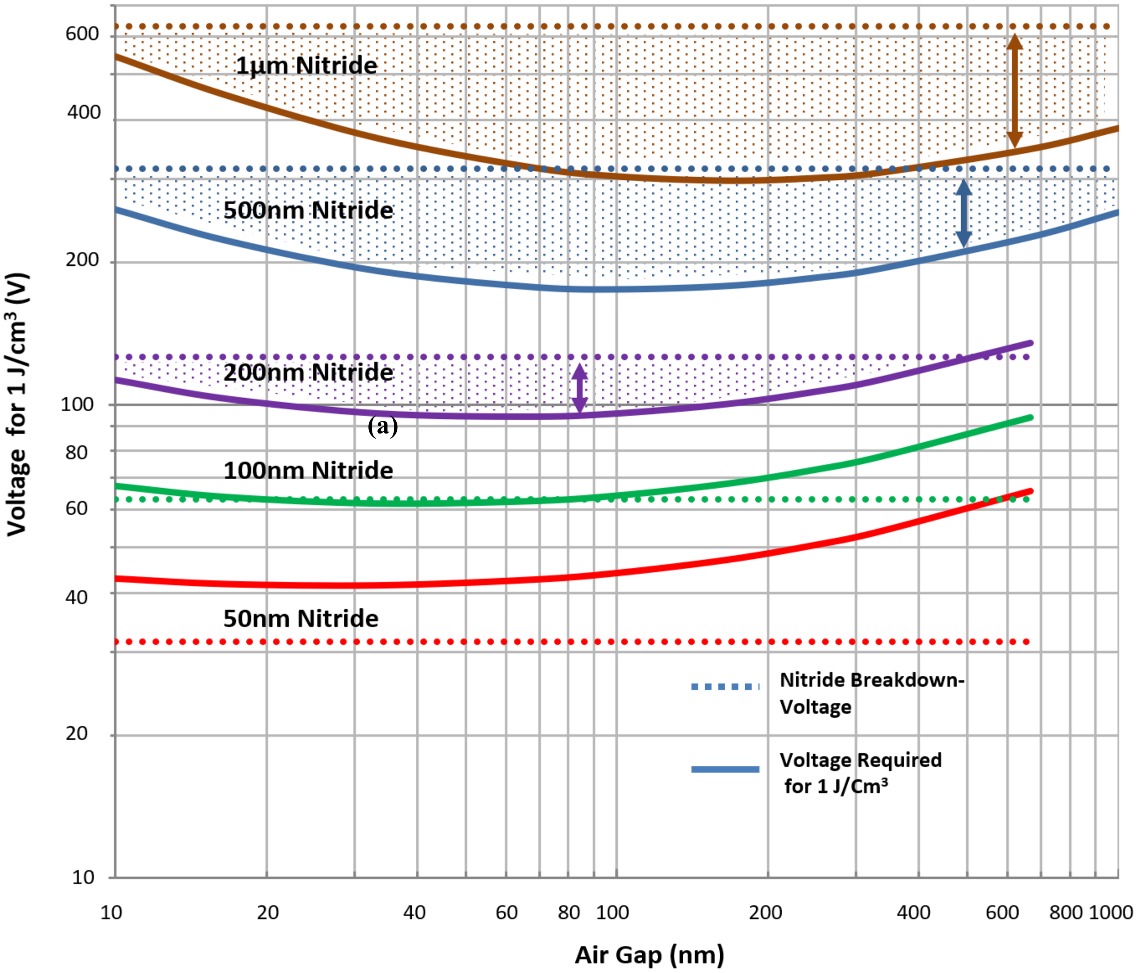

Figure 3.5. Actuation voltage required for 1 J/cm^3 versus air-gap size for different sidewall dielectric (nitride) thicknesses with artificial muscle minimum feature size of 1 µm; field of 6.3 MV/cm. Highlighted areas show the feasible range (required voltage below maximum voltage).

This is mainly due to the fact that the airgaps determine maximum strain in the actuators and even though more force can be produced by a narrower gap, the reduced range of motion lowers the amount of work performed by the actuator. The optimal range for the air-gap size based on figure 3.4 seems to be around 25% to 50% of the dielectric thickness. Also, based on Figure 3.6, for minimum feature size of 1µm, for nitride thickness of below 100 nm, the required voltage will be above the 6.3 MV/cm limit assumed for nitride breakdown.

Figure 3.6 shows the required actuation voltage as a function of the cell minimum feature size for different dielectric thicknesses, with the airgap having the same size as the dielectric thickness. As shown in this graph minimum feature size is a significant factor in achieving large energy

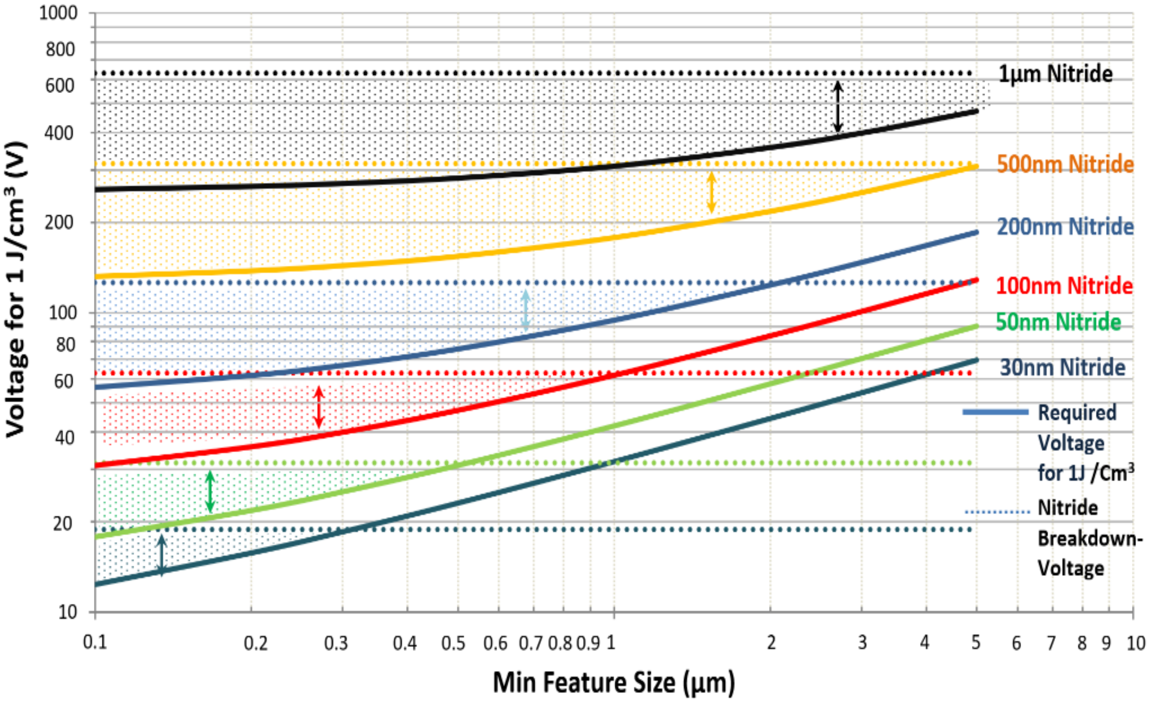

Figure 3.6. Actuation voltage required for 1 J/cm^3 versus minimum feature size for nitride thicknesses with air-gap size equal to nitride thickness. The dotted line for each graph shows the maximum actuator rated voltage limited by nitride breakdown field of 6.3 MV/cm. Highlighted areas show the feasible range (required voltage below maximum voltage).

densities at lower voltages. This is due to the fact that minimum individual cell width is a direct function of the minimum feature size available in defining the silicon mesh and the polysilicon openings within the mesh. Smaller cell width means larger muscle strain for the same air-gap size. As shown in figure 3.6, actuation voltages below 20V are achievable for minimum feature size of 0.1 µm. While such lithography resolutions are rather trivial in today's CMOS industry, the limit of optical lithography available to the PI's group is around 1 µm. Therefore, two approaches of e-beam lithography and multi-polysilicon trench refills (discussed in section B.3) are proposed and will be examined under this project to reach deep submicron minimum feature sizes.

3.2.6 POLYSILICON ELECTRODE STIFFNESS

One of the considerations in the design of cell actuator is the stiffness of the polysilicon electrodes versus the stiffness of the silicon structure they are to attract upon actuation. For optimal operation of the actuator it is desirable for the electrodes to be significantly stiffer than the silicon walls so that it is the walls that are pulled towards the electrodes and not the other way around. The polysilicon electrodes are however anchored to the silicon mesh at its nodal locations only on top of the substrate and the part of the polysilicon electrode extending into the deep trench is fully unsupported. Therefore, it is preferable for the electrodes to be much thicker than the silicon sidewalls. It should be noted, however, that although electrodes pulling into the sidewalls is not optimal, an actuator with inadequate electrode stiffness should still be operational. Once the electrode is pulled into the sidewall on one side, its airgap with the other sidewall increases requiring a higher voltage to produce the same amount of force.

3.3 FABRICATION

A modified version of the High Aspect Ratio Poly and Single-crystalline Silicon (HARPSS) fabrication process [56-59] will be developed to implement the proposed arrayed cellular electrostatic actuator on SOI substrates. The HARPSS process is uniquely capable of producing submicron high aspect ratio transduction gaps between tens to hundreds of microns tall silicon structures and polysilicon electrodes.

Figure 3.7 shows the schematic cross-sectional view of the proposed process flow for implementation of arrayed cellular electrostatic actuator integrated. The process starts by deep reactive ion etching (DRIE) of vertical trenches into the silicon device layer (50µm thick) of an SOI substrate. Trenches should extend all the way through the device layer ending at the SOI buried oxide layer (BOX) (Figure 3.7(a)). This step defines the silicon mesh for the arrayed cellular electrostatic actuator while keeping the silicon device layer around the actuator intact (the mesh is still part of the surrounding device layer). A layer of high quality conformal low stress silicon nitride (400nm) is then deposited via LPCVD covering the sidewalls. A high temperature anneal step in nitrogen [59], or oxidation and oxide removal steps may be performed prior to this step to remove the surface roughness (scalloping and striations) induced on the silicon sidewalls by DRIE. A layer of conformal silicon dioxide (250nm) is then deposited via LPCVD serving as the sacrificial layer defining the transduction air-gap size for the actuator cells (Figure 3.7.(b)). A 7µm thick layer of LPCVD p-doped polysilicon is then deposited that refills the trenches and forms the vertical electrodes. It has been demonstrated that the polysilicon needs to be annealed at high temperature. Annealing at 1100 degree improves the diffusion of dopant in the polysilicon. If it is determined that adding a nitride layer on the polysilicon surfaces can further enhance the air-gap

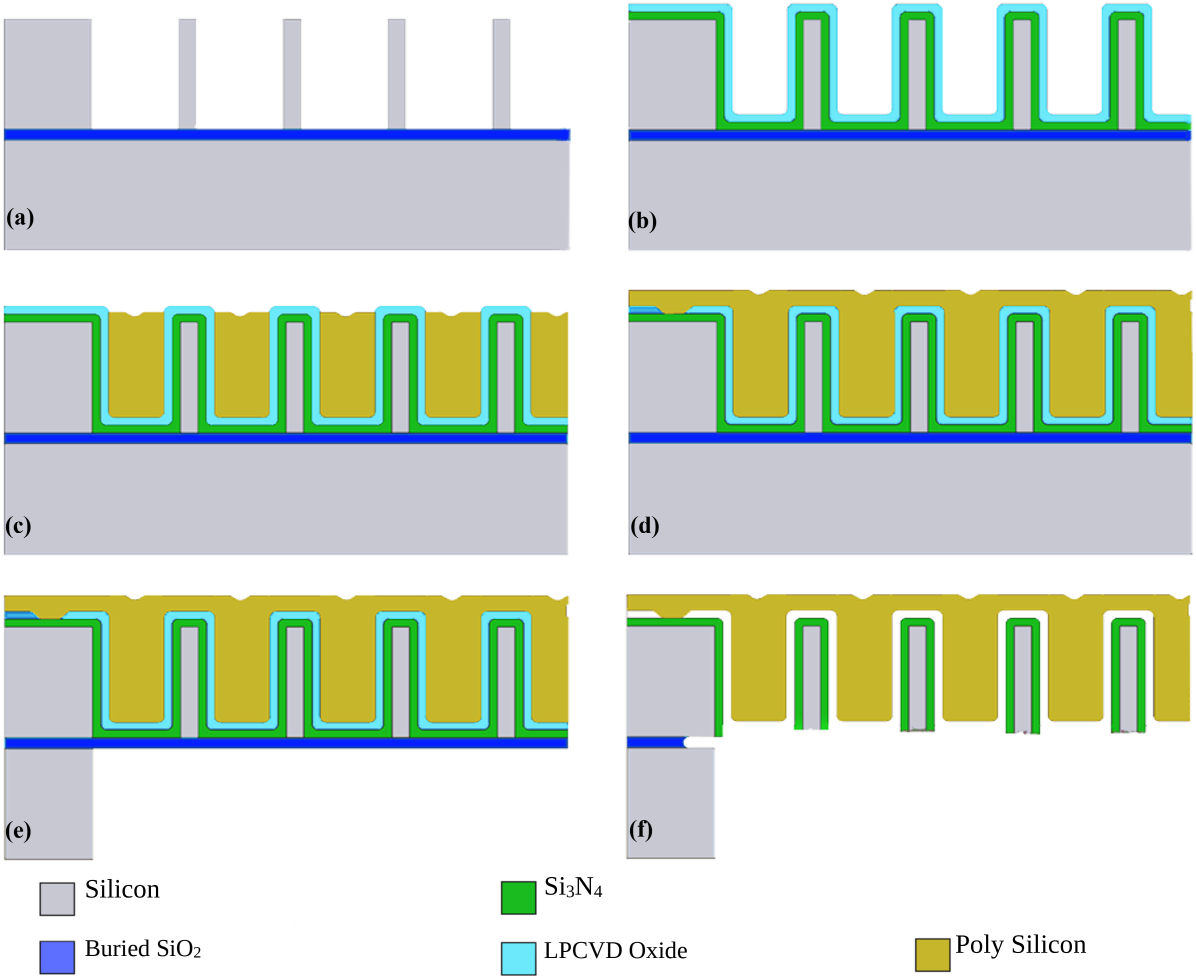

Figure 3.7. Schematic cross-sectional view of the modified HARPSS process flow for fabrication of arrayed cellular electrostatic actuators

breakdown voltage, another LPCVD nitride deposition step can be added before polysilicon deposition. Polysilicon is then etched back on the top surface (Figure 3.7(c)) providing access to the silicon dioxide sacrificial layer so that it can be selectively patterned and removed from certain areas where the electrodes are to be anchored onto the silicon mesh. A second layer of doped LPCVD polysilicon is then deposited to be patterned providing interconnects between polysilicon electrodes and forming electrode anchors to the silicon frame (at nodal points where deformation of the frame is close to zero) (Figure 3.7(d)). The nitride layer provides electrical isolation between the anchored polysilicon and silicon substrate.

The arrayed cellular electrostatic actuator has relatively large sizes in the few millimeters range, therefore, to avoid stiction and minimize the time required to undercut structures (during BOX layer removal at the end of the process), the silicon handle layer needs to be patterned and removed underneath large components. For this purpose, a backside lithography step and long handle layer DRIE is to be performed (Figure 3.7(e)). Upon complete removal of the silicon handle layer in the required areas, the BOX layer as well as the silicon nitride layer on the bottom of the trenches are to be removed via plasma etching. It is generally preferable not to perform any topside lithography steps after removing large areas of the handle layer as partial removal of the handle layer makes the whole substrate fragile. It is therefore expected that a hard mask (likely silicon dioxide) is deposited (or grown) and patterned on the 2nd polysilicon layer, before performing the backside processing.

After patterning the silicon handle, topside processing resumes by etching the second polysilicon layer. During the same step, the silicon device layer around the arrayed cellular electrostatic actuator structures is also removed defining the outline of the silicon meshes as well as forming the supporting tethers. Finally, the sacrificial oxide between the silicon and polysilicon sidewalls within the deep trenches is removed by a hydrofluoric acid (HF) dip that could last up to 30 minutes depending on the trench depth and thickness of the sacrificial layer (Figure 3.7(f)). Silicon nitride has a very low etch rate in HF and therefore, most of the thickness of the nitride layer covering the silicon and/or polysilicon sidewalls is expected to remain in place.

3.4 FINIT ELEMENT ANALYSIS AND EXPERIMENTAL RESULTS

3.4.1 IN PLANE ACTUATION RESULTS

Figure 3.8 shows a fabricated arrayed cellular electrostatic actuator with 242 rows and 9 or 10 cells per each row (total of 2299 cells). Zoomed in view of the flexible suspended polysilicon interconnects, and their anchoring points to the silicon frame are also shown in Figure 3.9. Each cell is 95µm long and 8µm wide. Overall size of the entire array is 2010 µm by 1010 µm. Figure 3.10 (a) shows the zoom in view of one end of the device at rest and figure 3.10(b) shows the open-air gap of 240nm. Figure 3.10(c) shows the SEM view of the same device upon application of a 35V applied between silicon skeleton and polysilicon electrodes. As expected, the silicon skeleton has been contracted due to the overall lateral electrostatic force pulling the silicon skeleton towards the polysilicon electrodes. Axial displacement at the tip of the actuator is

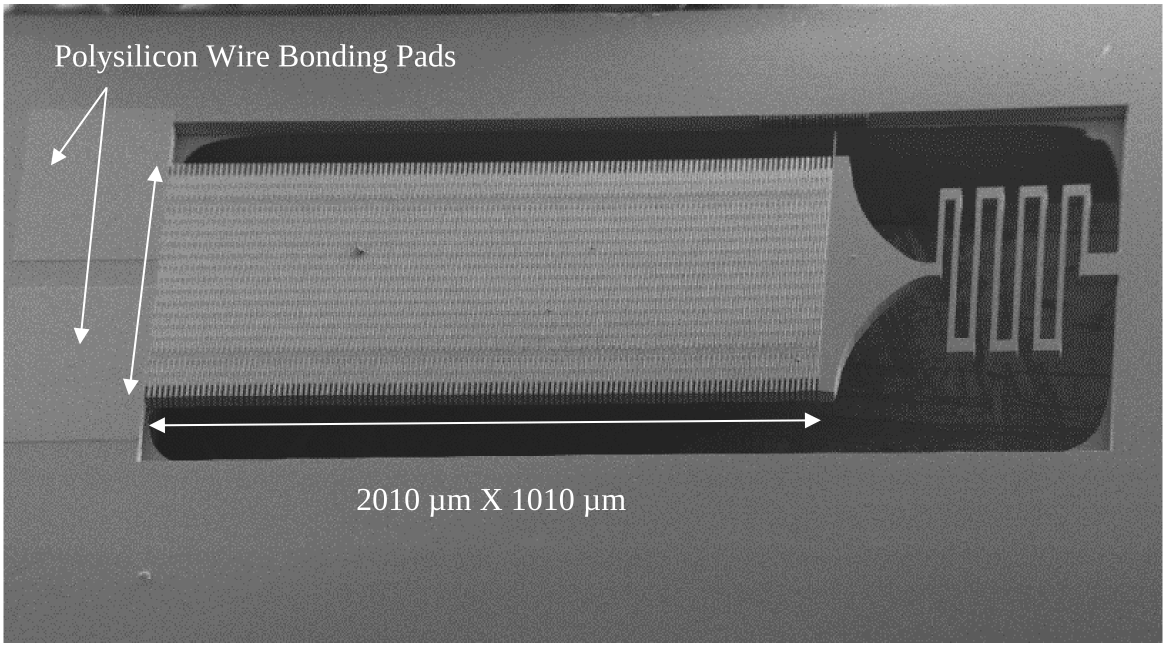

Figure 3.8. SEM images of fabricated 2010 m x1010 arrayed cell actuator showing full view of the array

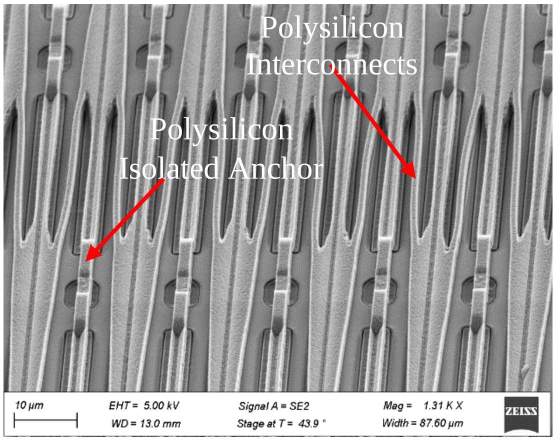

Figure 3.9. SEM view of polysilicon interconnect along with polysilicon anchor point to the silicon mesh.

estimated from SEM view to be 20.5 µm up to 35V of actuation voltage. This overall contraction of the actuator results in linear strain of 1%. To achieve this strain, each airgap of each cell has

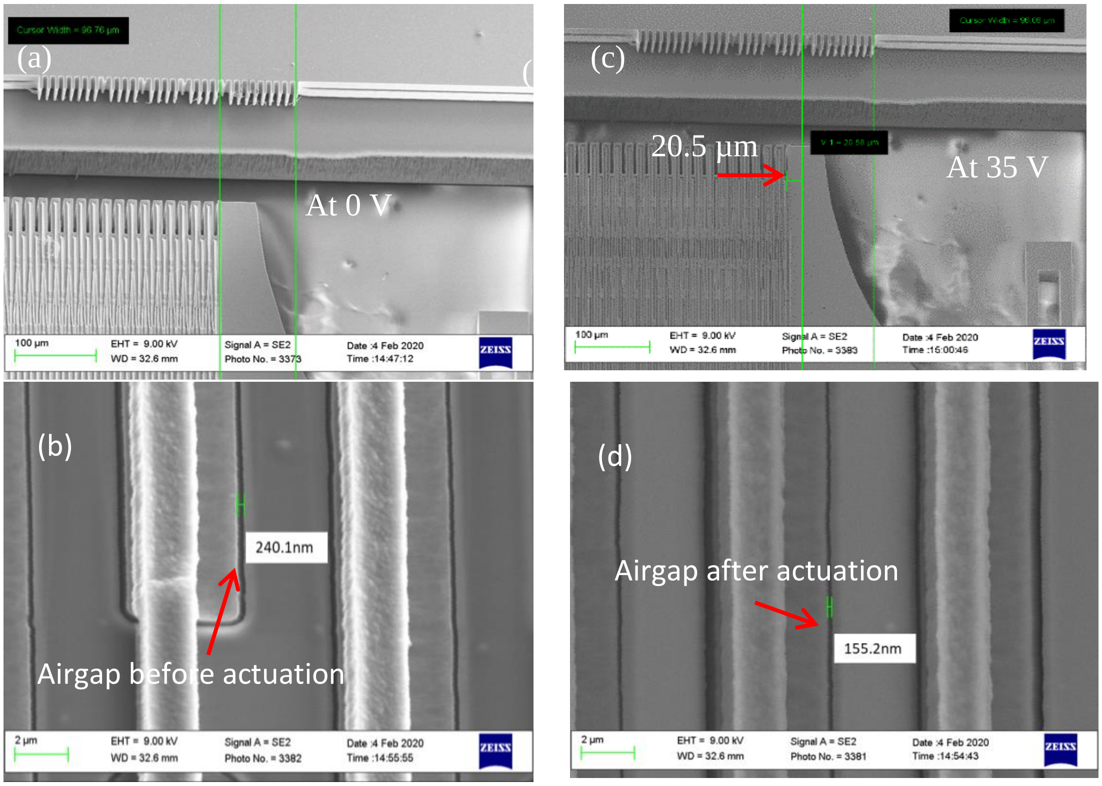

Figure 3.10. (a). Zoomed in view of one end of the device at rest, (b) Zoomed-in view of the open airgap, (c) SEM view of the one end upon the application of actuation voltage, (d) Zoomed-in view of the closed airgap upon the application of actuation voltage 35 V.

been reduced by 85 nm. Figure 3.10 (d) shows the closed air gap of one side of a cell. According to finite element analysis (FEA) results (figure 3.11.(a)), the mechanical stiffness of each cell is 7000N/m. Using given stiffness and displacement, the work performed by each cell is 0.16nJ obtained from Hook's Law i.e.

$$w = \frac{1}{2}kx^2 \tag{3.3}$$

where the k is the mechanical stiffness, x is the displacement of the Based on the law of conservation of energy, work done by the entire device is a summation of the work done by each cell, i.e.

$$w_{entire\ device} = w_{one\ cell} . N_{number\ of\ cells} \tag{3.4}$$

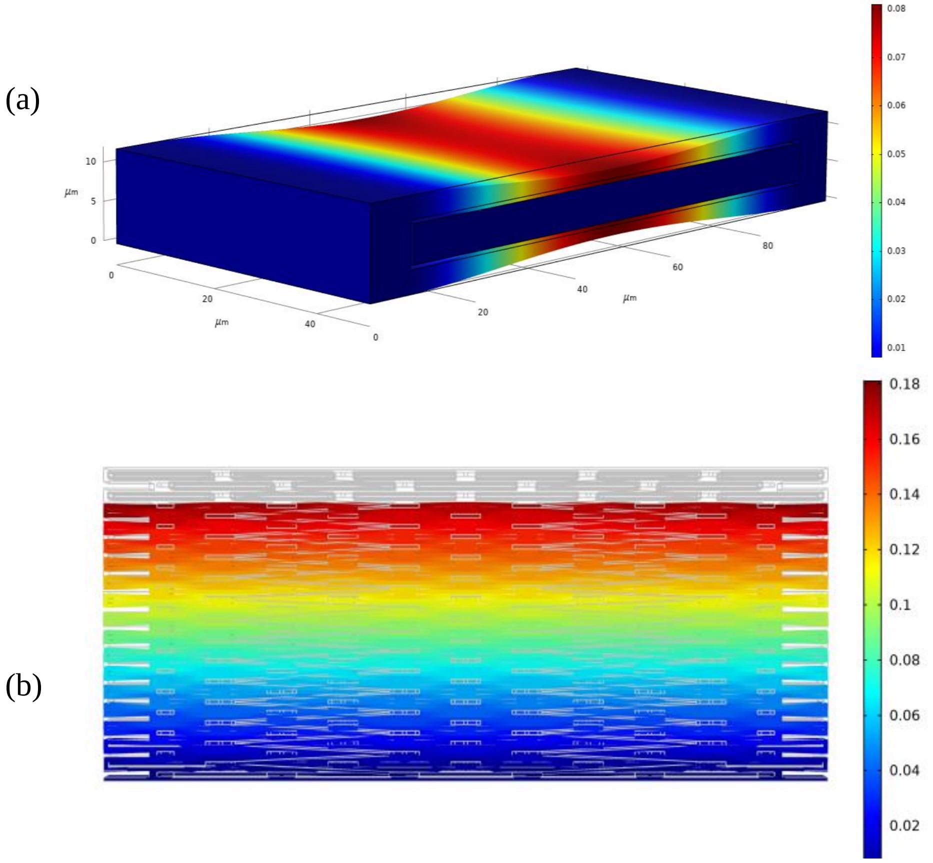

Figure 3.11.(a). Displacement profile of single cell upon the application of actuation voltage (35v). (b) Displacement profile of a cellular arrayed actuator (20 rows by 5/6 cells in each row) upon the axial stress.

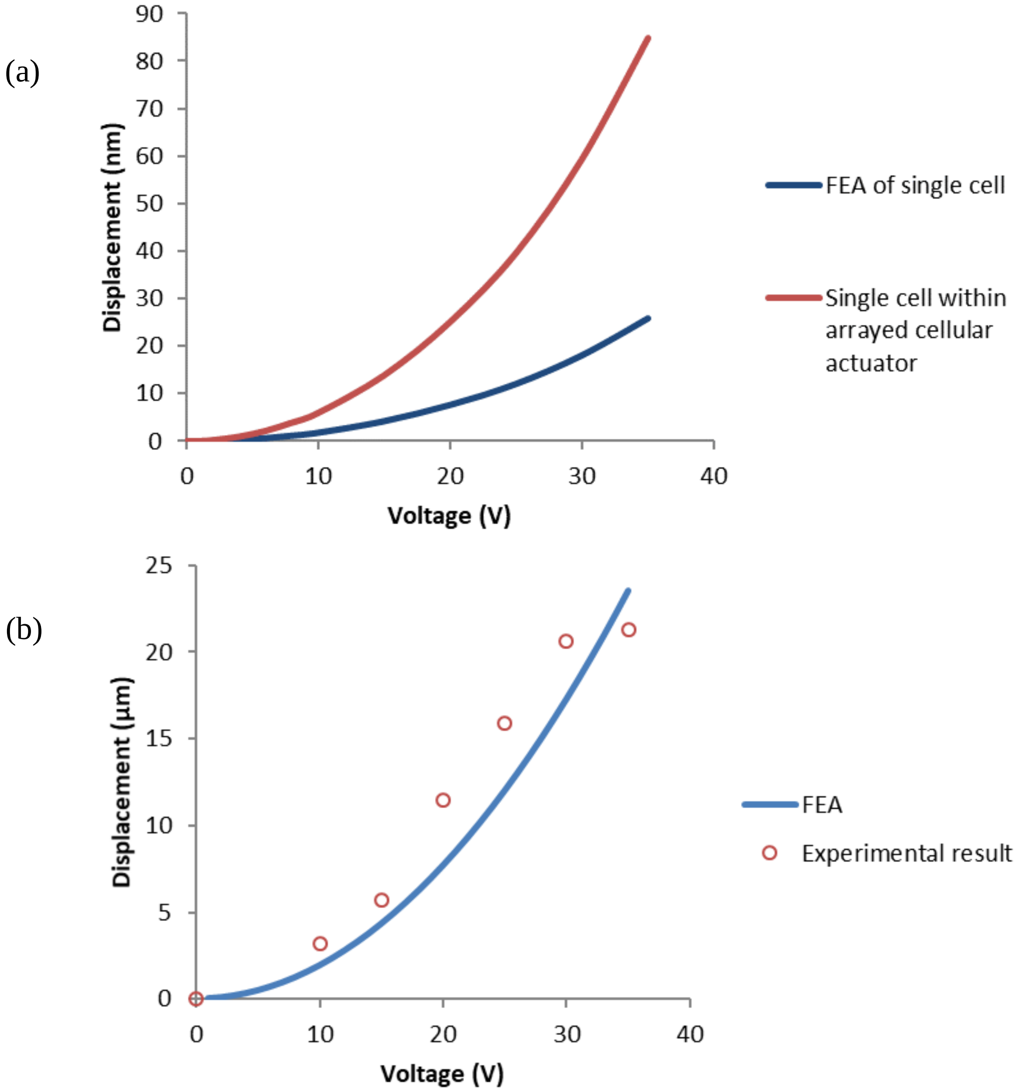

Figure 3.12.(a). Displacement vs Actuation Voltage for single cell. (b) Displacement vs Actuation voltage for tested 2mm × 1mm device along with FEA result.

By multiplying the number of the cells within the tested device of 2299, the expected work of arrayed cellular electrostatic actuator is 0.24µJ. The blocking force at the tip of the actuator can be obtained from the Hook's law, where the axial stiffness of 1166N/m results in blocking force of 24mN at the tip of the actuator. The axial stiffness of the structure has been obtained from the FEA by using COMSOL 5.5 solid mechanics physics (figure 3.11(b).

Using Equation 3.1 and the given dimensions, the electrostatic force acting on the sidewalls of individual cell is around 1.08mN. Using equation 3.3 and 3.4, it has been demonstrated that the overall displacement of the tip of actuator is equal to summation of the displacement of the side walls of cells lined up in the length of the device. Also, the blocking force at the tip of the actuator is equal to the summation of parallel plate electrostatic force of cells acting on two ends of the device. Figure 3.12(a) shows the displacement vs actuation voltage of each cell within the arrayed cellular electrostatic actuator and single cell electrostatic actuator. This graph shows the displacement of each cell within the arrayed cellular actuator is larger than the displacement of the single cell electrostatic actuator. Figure 3.12(b) shows the displacement vs actuation voltage for the tested cellular arrayed electrostatic actuator.

The actuation voltage was limited to the breakdown voltage of the nitride film which was expected to be higher than breakdown voltage that we got during testing the device. This is an area of research for the upcoming design consideration. Along with the force and displacement of actuators, energy density of actuators can show the amount of work that the actuator can perform

Table 3.1. Performance of the tested device compared to some of the other works which recently reported in this area of research.

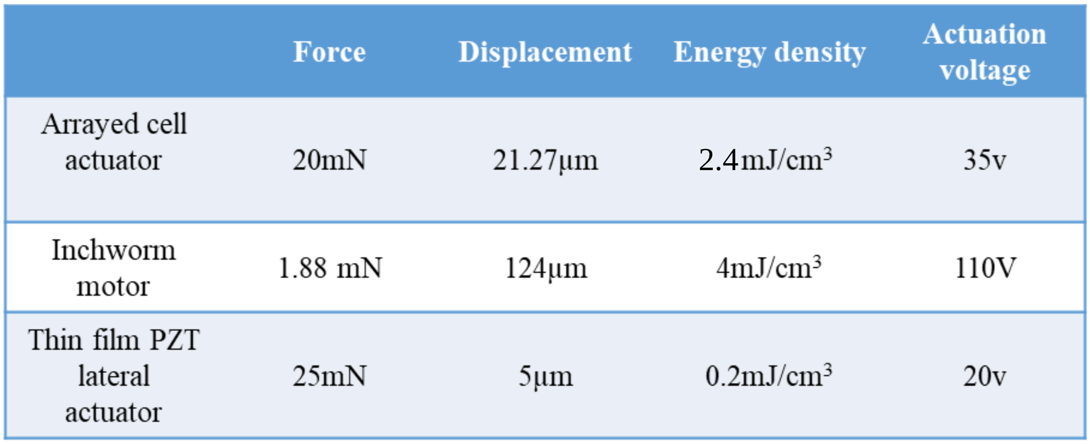

	Force	**Displacement**	**Energy density**	**Actuation voltage**
Arrayed cell actuator	20mN	21.27µm	2.4mJ/cm^3	35v
Inchworm motor	1.88 mN	124µm	4mJ/cm^3	110V
Thin film PZT lateral actuator	25mN	5µm	0.2mJ/cm^3	20v

which could be normalized per volume or mass of the actuator. The energy density of 2.4mJ/cm^3 is achieved by using the given dimension of the tested device and the work performed by the actuator (0.24µJ) upon the application of actuation voltage of 35V.

Table 3.1 shows the summary of performance of some of the relevant device in this research area in comparison to our tested device.

Additional to the axial displacement of the device, it has been demonstrated that using the different electrically isolated paths for polysilicon interconnects, either all the cells or the cells lined up in each half side of the Si skeleton can be actuated separately (figure 3.13.(a)). In this manner, in-plane rotational movement can be performed by actuating cells in one side of the

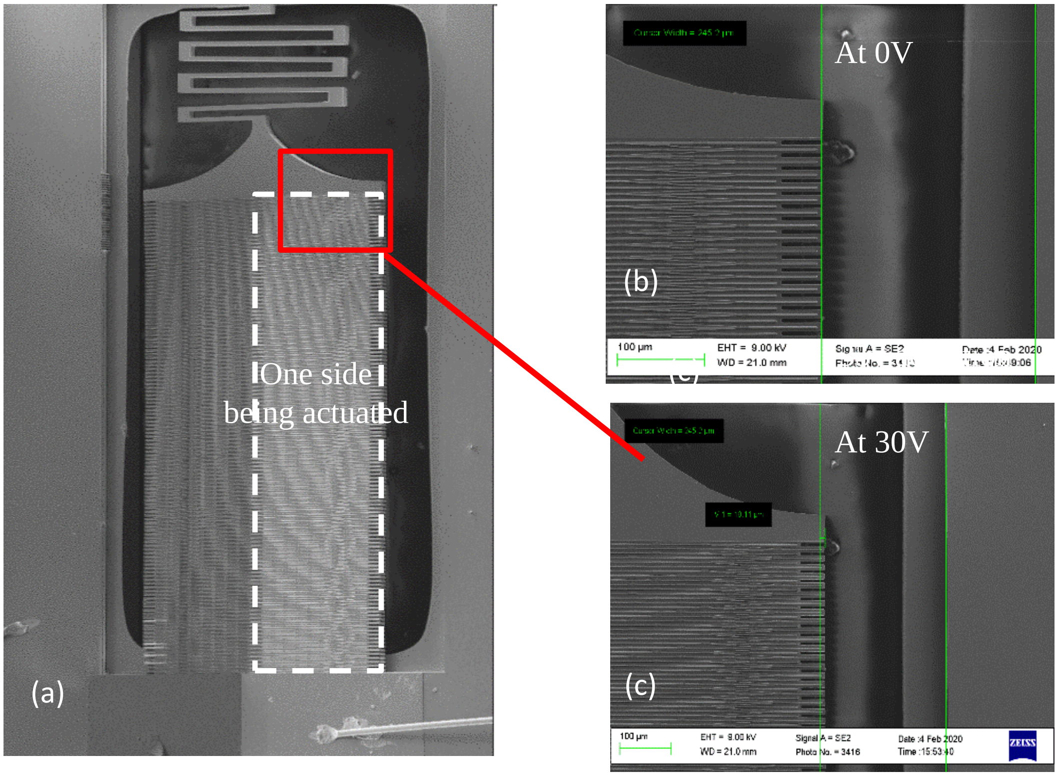

Figure 3.13.(a). SEM view of tested device with 2mm×1mm footprint with rotational displacement, (b), (c) SEM view of one end of the same device at rest and upon the application of actuation voltage, respectively.

actuator. Figure 3.13 (b) and 3.12 (c) shows the SEM view of the rotational movement of the actuator. The displacement of the tip of the actuator has been estimated from the SEM view of the actuator for 10 µm with actuation voltage of 35V.

3.4.2 OUT OF PLANE ACTUATION RESULTS

Further to in plane operation of the cellular arrayed electrostatic actuator, out of plane operation of the device has been studied. In order to get the out of plane displacement of the device a very

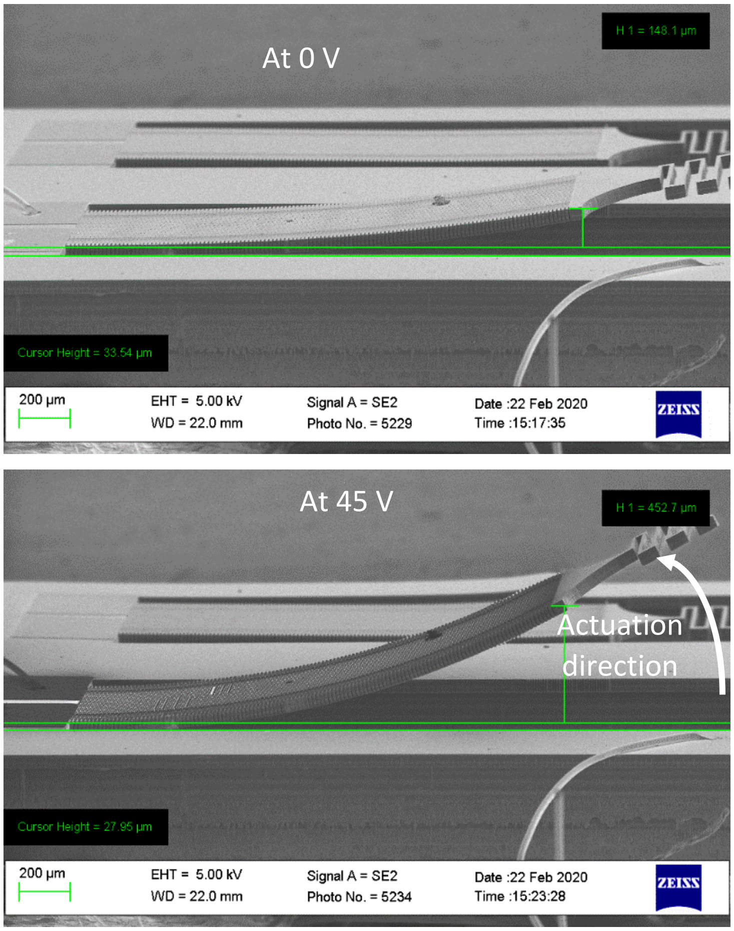

Figure 3.14. SEM view of arrayed cellular electrostatic actuator fabricated with modified process to get the out of plane actuation along with SEM view of the device upon the application of the 45V.

slight mechanical modification is required to be applied to the arrayed cellular electrostatic actuator. Keeping the thin film of nitride deposited during the fabrication process on the actuator bottom-side leads to an overall bending moment bending the actuator upwards. Figure 3.14 shows the SEM view of the modified device (with the same dimensions and number of cells comparing to the device tested for in plane actuation) upon the application of a 45 V actuation voltage. As expected, the device curves upwards taking the shape of an arch as it experiences a uniform bending moment along its length.

Due to the stress of the Nitride kept under the actuator, the device curved upward without application of actuation voltage for 148um. The bending resulted from stress of nitride film closed the airgaps of each cells for 12nm. Vertical displacement at the tip of the actuator is estimated from the SEM view to be ~460µm with 45V actuation voltage. Based on the measured displacement at the tip of the device, the radius of curvature for the curved actuator is 4.4mm (around 25-degree arch angle). To achieve such curvature, the structure should have shrunk by 20µm on its top surface, i.e. each of the airgaps in each cell should have been reduced by ~82nm at the top (155nm remaining airgap). Using Equation 3.1 and the given dimensions, the electrostatic force acting on the sidewalls of individual cells is around 1.03mN. With flexural stiffness of 3.3N/m at the tip of the actuator obtained from FEA using COMSOL 5.5 solid mechanic physics, and vertical displacement of 452µm, the vertical force at the tip is obtained to be around 0.9mN using Hook’s law force-displacement equation for a given stiffness.

Using the flexural stiffness of the actuator and given dimensions of the device, the effective Young’s modules of the composite structure can be given by:

$$E_{effective} = \frac{4kl^3}{wt^3} \qquad (3.5)$$

where the $E_{effective}$ is the effective Young's modules of the composite structure of arrayed cellular electrostatic actuator, k is the flexural stiffness of the device, and l, w and t are the length, width and thickness of the device, respectively. The effective Young's modules of 301MPa has been obtained for the tested device using formula 3.5. The bending moment of

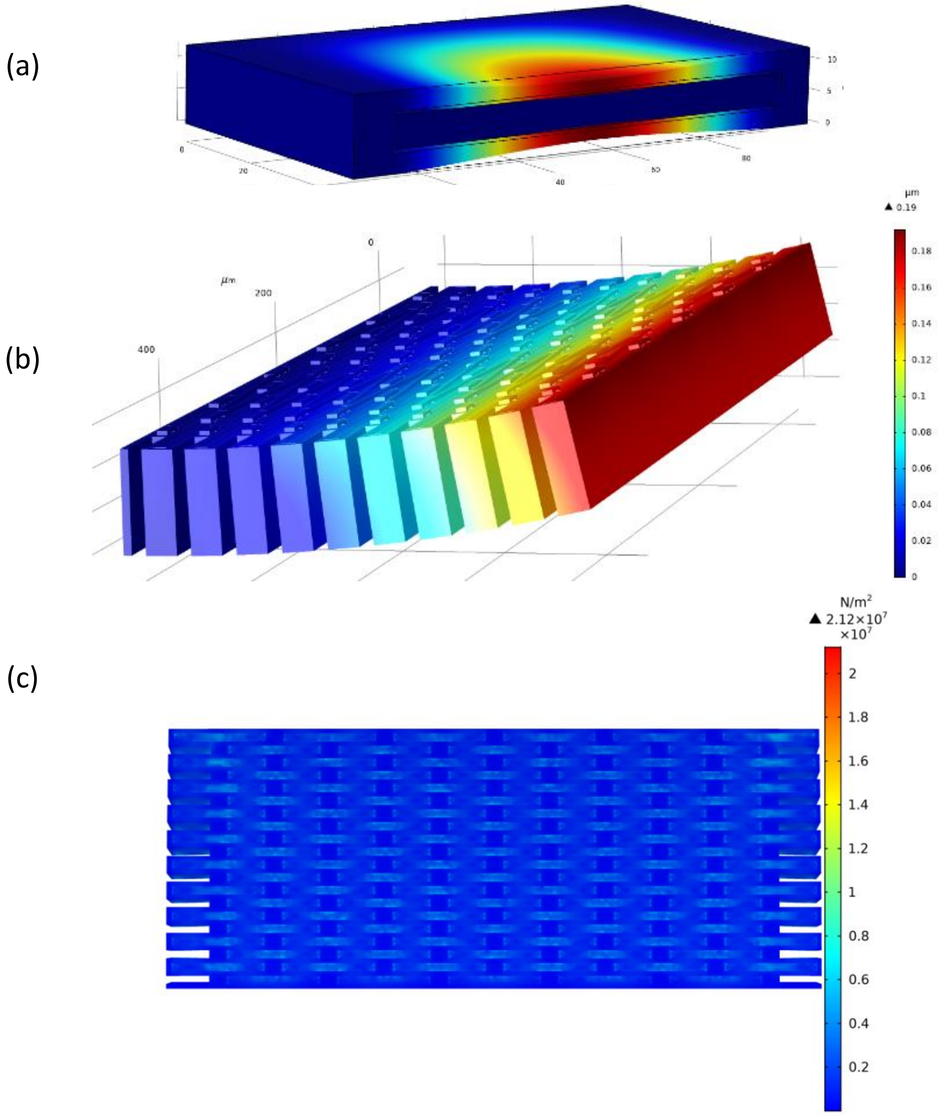

Figure 3.15.(a). Displacement profile of single cell upon the application of actuation voltage (35v). (b) Displacement profile of a cellular arrayed actuator (20 rows by 5/6 cells in each row) due to the bending moment, (c) Stress profile showing relatively uniform stress due to the bending moment.

the curved structure upon the application of actuation voltage can be obtained by the effective Young's modules, radius of curvature and the moment of inertia. i.e.

$$M = \frac{1}{R}\, E\, I \qquad (3.6)$$

where the M is the bending moment, R is the radius of curvature, and I is the moment of inertia.

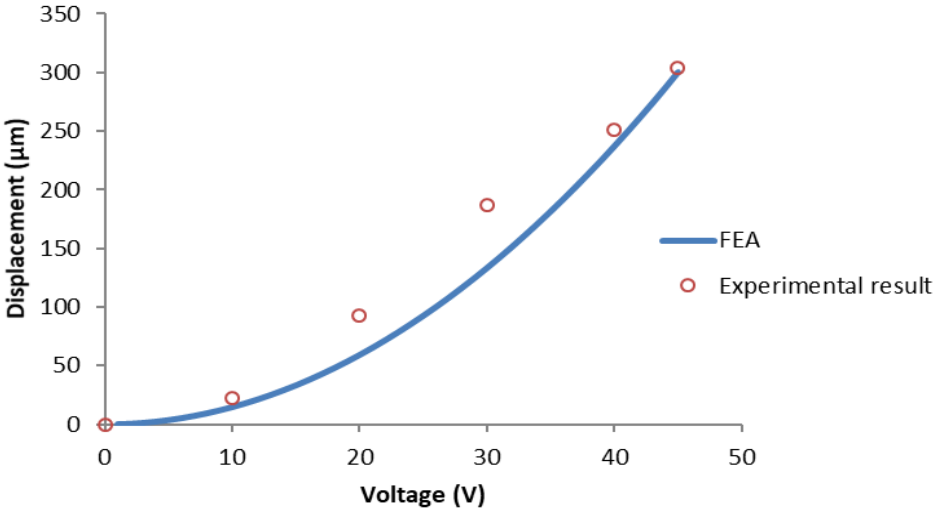

Figure 3.16. Displacement vs Voltage for 2 x 1 out of -plane actuation along with FEA results.

Figure 3.15 (a) shows the displacement profile of the single cell upon the application of a selected actuation voltage. Figure 3.15 (b), (c) show the displacement profile and stress profile of the similar structure with a selected number of cells. Physical memory of the system used for running the simulation limited the number of the rows and cells of the device used for FEA. At the end the FEA results scaled up in a proper manner to estimate the flexural stiffness of the actual device. Figure 3.16 shows the displacement of the tip of the device vs the actuation voltage. The graph shows a good match between the FEA results and experimental results for selected actuation voltages.

Table 3.2. Out of plane performance of the tested device (with 2mm×1mm footprint) compared to some of the other works which recently reported in this area of research.

	Force	Displacement	Energy density	Actuation voltage
Arrayed cell actuator	0.9mN	304µm	1.47mJ/cm^3	50v
Electrostatic piston tube	59µN	28µm	178µJ/cm^3	80V
PZT with leverage Mechanism	16mN	6.3µm	0.23mJ/cm^3	170V

Table 3.2 shows a performance of the of the tested device compared to some of the other works which recently reported in this area of research.

Furthermore, a piece of Si with mass of 8 mg was used to observe the weight lifting and throwing capability of the actuator. Figure 3.17 shows the actuator lifting the 8mg weight, which is about 60X times heavier than the actuator itself. The weight is lifted by around 200 µm

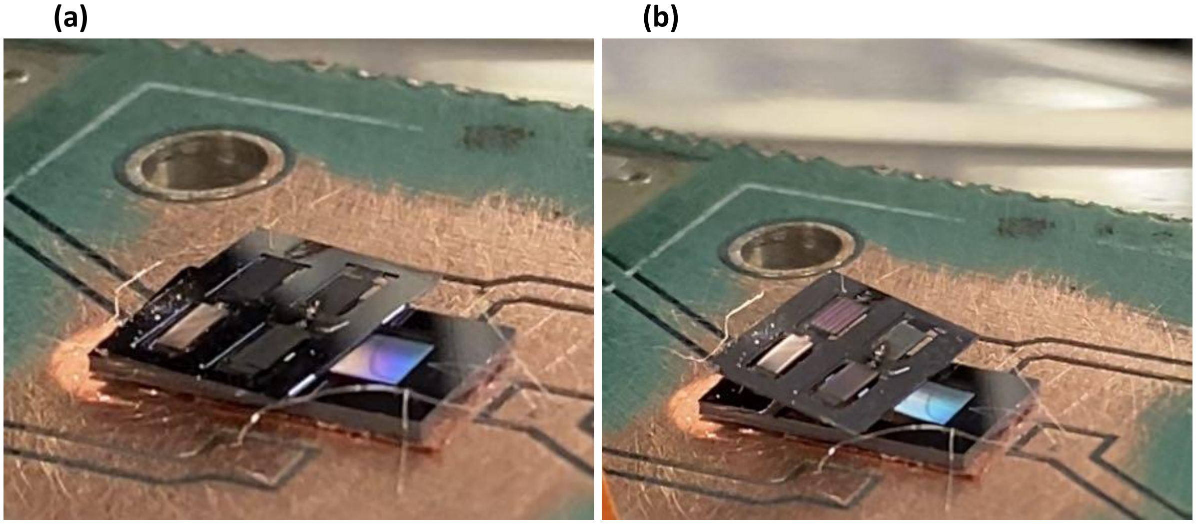

Figure 3.17. Pictures of a lifted mass of 8mg with 50V actuation voltage.

(estimated from the picture) with actuation voltage of 45V. Further lifting was not possible due to the mass rolling and falling off of the actuator surface.

In order to improve the performance of device, different arrayed cellular electrostatic actuators have been designed and fabricated with the similar operation principle and fabrication process. With the new designs, the cell dimensions have been modified to achieve higher force and displacement. Figure 3.18 shows SEM view of a fabricated cellular electrostatic actuator array with 362 rows and 20 or 21 cells per row in alternative rows (total of 7421cells). Each cell is 95µm long and 11µm wide. Overall size of the entire array is 3982 µm by 1995µm. The Figure 3.18 shows a upward displacement of 1124 µm (estimated from SEM view) upon the application of 46V. Figure 3.19 shows the displacement (tip of the device) vs actuation voltage. The graph shown

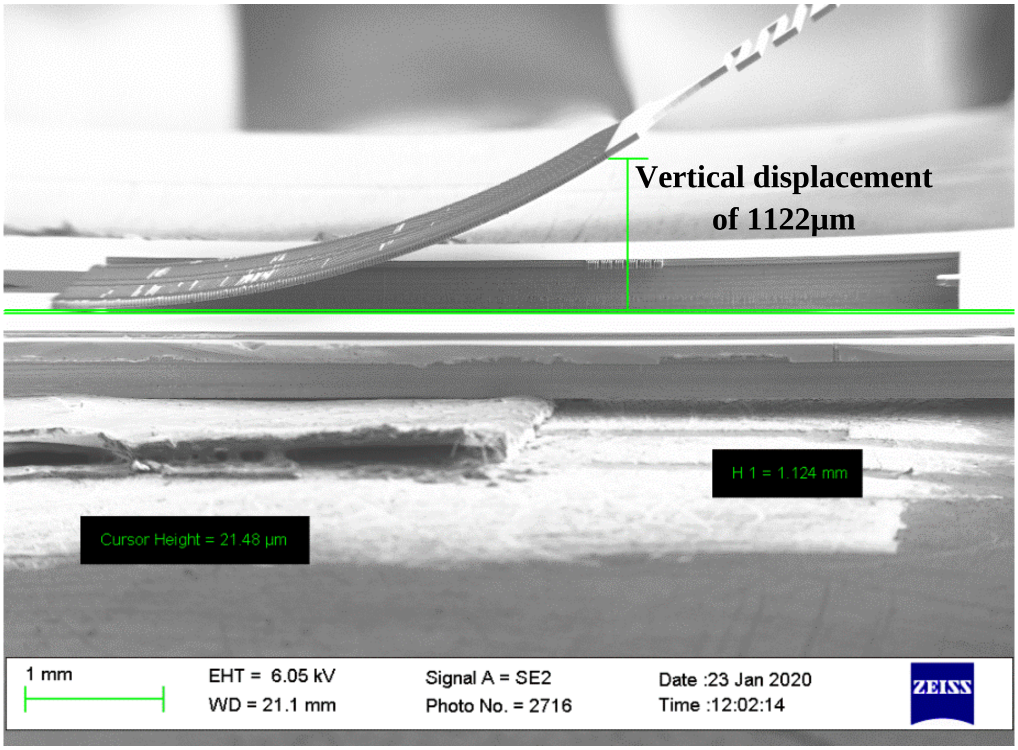

Figure 3.18. SEM view of bent device (4mm×2mm footprint) upon the application of 46V.

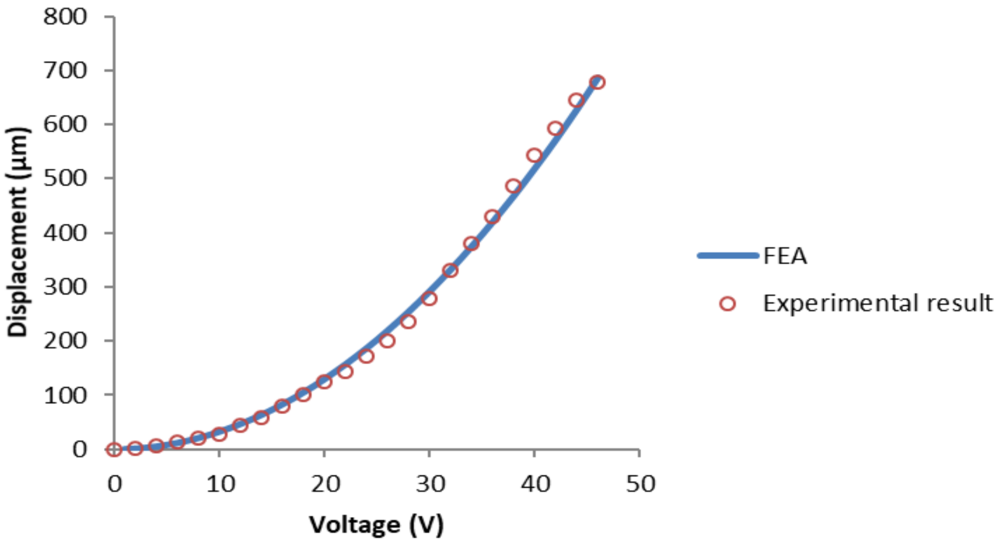

Figure 3.19. Displacement vs Voltage for 4mm x 2mm out of -plane actuation along with FEA results.

in figure 3.19 shows a good fit between FEA results obtained from COMSOL simulation and experimental results for selected actuation voltages.

Table 3.3 shows the summary of device descriptions and tests results for 3 successfully fabricated and tested arrayed cellular electrostatic actuators. The effective Young's modulus, flexural stiffness of each device shown in the table have been obtained from FEA results and analytical calculation using the given formula in this chapter.

Table 3.3. Showing description and mechanical characteristics of three tested devices along with their performances upon the application of actuation voltages.

Device footprint	*2 mm × 1 mm*	*2 mm × 2 mm*	*4 mm × 2 mm*
Cell length	80µm	80 µm	80 µm
Side-wall width	3 µm	4 µm	4 µm
Polysilicon electrodes width	5 µm	7 µm	7 µm
Thickness of device	50 µm	50 µm	50 µm
Vertical displacement upon actuation voltage	304 µm	332.7 µm	678 µm
Flexural Stiffness of device	3.4N/m	14.2N/m	1.8N/m
Effective Young's Modulus	301 MPa	675 MPa	675 MPa
Actuation voltage	45 V	60V	46V
Force at the tip of the device	0.9mN	4.7mN	1.22mN
Bending moment	$7.8*10^{-7}$Nm	$3.3*10^{-6}$Nm	$1.925*10^{-6}$Nm
Radius of curvature	4417.9 µm	4255.3 µm	7272.7 µm

3.5 SUMMARY AND FUTURE WORKS

Submicron high aspect ratio transduction airgaps produced via the HARPPS process in combination with the cellular array structures enable implementation of micro-machined high force electrostatic actuators with a wide range of motion. It has been demonstrated that arrayed cellular electrostatic actuators can offer significantly larger displacement and work output per volume compared to the conventional MEMS actuators. Also, performance of such devices has been demonstrated for 3 degrees of freedom including axial, rotational, and vertical displacement.

A fabrication modification has been needed to achieve the vertical displacement.

Future work includes demonstration of larger actuation arrays with narrower airgaps leading to lower operating voltages and/or higher force/work output and utilization of such in micro-robotic platforms micro lens actuator module.

CHAPTER 4

SIDE PROJECT

4.1 THERMALLY ACTUATED METAL RESONATOR PIEZORESISTIVE RESONANT MASS BALANCE IMPLEMENTED IN CMOS PROCESS [1]

This work presents implementation of electro-thermally actuated MEMS resonators in a standard CMOS process via addition of a few mask-less post-processing steps. The resonators are made of CMOS interconnect metal (Aluminum and Tungsten) and insulation layers (silicon dioxide) and utilize two sets of electrically isolated metal double layers for thermal actuation and piezoresistive readout. The oxide layers within the resonator structures lead to an improved temperature coefficient of frequency (TCF) of -2.7 ppm/˚C (~10X better than silicon). The fabricated resonators were embedded in a custom-made miniature aerosol impactor collecting and measuring the mass concentration of airborne particulates. Tests performed on air samples from different sources with different particle mass concentrations ranging from 0.014-0.085 $\mu g/m^3$ show a clear correlation between the mass balance frequency shifts and the expected particle concentrations.

4.1.1 INTRODUCTION

The high cost associated with process development and manufacturing of MEMS is one of the major hurdles for commercialization of new MEMS-based products. This can be bypassed by

---

[1] © 2018 IEEE. Reprinted, with permission, from Abbasalipour, Amin, Varun Kumar, Alireza Ramezany and Siavash Pourkamali, "Thermal Piezoresistive Resonant Mass Balance Implemented in a Standard CMOS Process," 2018 IEEE International Frequency Control Symposium (IFCS), Olympic Valley, CA, 2018, pp. 1-4, DOI: 10.1109/FCS.2018.8597576.

formation of the main bulk of the MEMS via a standard CMOS process. Furthermore, the flexibility offered by multiple interconnect layers in a CMOS process, as well as the ability to integrate circuitry along with the MEMS are unmatched advantages of this approach.

Mass concentration of airborne particulate matter (PM) is one of the major factors in air quality with various health implications, including early death in people with heart or lung disease, nonfatal heart attacks, irregular heartbeat, and aggravated asthma [60]. Additionally, airborne PM concentration is a growing area of concern in many industries, where a very high air quality is needed, such as semiconductor manufacturing. In particular, aerosol contaminants in semiconductor and electronics manufacturing cleanrooms can limit the minimum feature size of integrated circuit elements [61]. Therefore, continuous monitoring of air quality in urban areas as well as the industrial sites can significantly help maintain the desirable air quality level. A variety of aerosol sampling and particle counting techniques have been developed over the past decades, including dielectrophoresis [62], deterministic lateral displacement (DLD) [63], hydrophoretic separation [64]. Routinely, these methods are not suitable for nanoscale particle detection. On the other hand, optical particle counters operating based on reflection of scattered light by particles passing through a laser beam, have been developed as the most common system for measuring and analyzing the air suspended particle during the last decades [65]. Higher end versions of such systems utilizing higher-intensity and lower-wavelength laser sources can detect particles down to 0.1 μm but If they can to some extent [66].

Additionally, integration of MEMS resonators with cascade inertial aerosol impactors has been demonstrated for real time monitoring and mass concentration measurement of airborne particulate matter [67], [68]. In this manner, microelectromechanical silicon based thermally actuated dual-plate resonators with piezoresisitive readout have been demonstrated as highly sensitive sensors for a wide variety of applications, some of which are pressure sensor [69], sheer stress sensors [70], Lorentz force MEMS magnetometer [71], frequency output force and displacement sensor [72], as well as PM monitoring [73]. In this work, a metal based dual-plate resonator implemented on a CMOS chip has been investigated as a compact solution for PM monitoring capable of integrating with the state-of-the-art electronics.

4.1.2 DESCRIPTION

The dual-plate resonators used in this work are comprised of two suspended plates connected by a narrow beam in the middle. The resonator patterns are formed in the CMOS chip metal-insulator stack (Figure 4.1) by including the desirable patterns in the chip layout during tape-out. Insulated metal layers embedded within the narrow beam act as thermal actuators and piezoresistive detectors for operation of the device. Electrically connected metal layers 1 and 3 were configured as the input to act as thermal actuators. Upon thermal actuation of the beam at the natural frequency of the resonator, the suspended plates vibrate back and forth in an in-plane resonance mode, while the beam undergoes a periodic longitudinal stress and produces a piezoresistive readout signal, with metal layers 2 and 4 used for piezoresistive readout. For PM measurements, the resonators were embedded within different stages of a miniature 2-stage cascade impactor to collect the incoming particles with different sizes. The cascade impactor is comprised of two machined aluminum chambers which have precisely drilled nozzles as air inlets. A miniature vacuum pump is used as the source for the air flow required for particle collection. The cascade impactor is comprised of two machined aluminum chambers which have precisely drilled nozzles as air inlets. A miniature vacuum pump is used as the source for the air flow

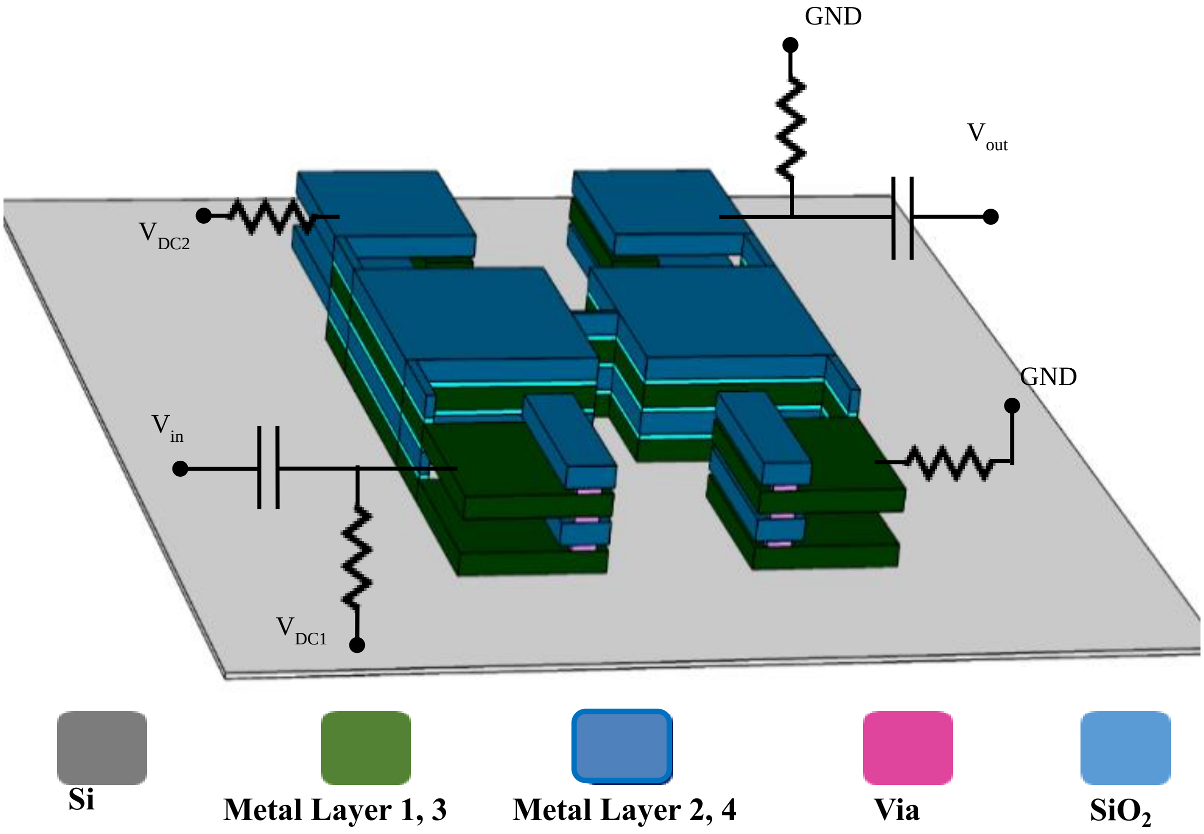

Figure 4.1. Schematic view of a dual plate thermal piezoresistive resonator implemented in the CMOS process showing the different metal layers wherein metal layers 1 and 3 and metal layers 2 and 4 are electrically connected

required for particle collection. In each stage aerosol stream passes through the nozzles and impinges on the impaction plates. Particles with larger inertia will impact on the plate,

while small particles scape from impact and will go to the second stage. By designing each stage with higher aerosol velocity in the nozzles, smaller particles will be collected at each stage [14]. Particle mass deposition on the plates will increase the mass of the resonator and in turn reduce its resonance frequency.

4.1.3 POST-CMOS FABRICATION

Chips were fabricated in a standard CMOS process. Large vias strategically placed in the CMOS layout around the cantilevers were then wet etched by dipping the chips successively in warm (50^{o}C) Aluminum etchant and Hydrogen Peroxide (Tungsten etchant) until the field oxide layer was reached. The field oxide underneath the metal stack (~500nm) acts as a perfect etch-stop for these acids due to the high selectivity of Aluminum etchant and Hydrogen peroxide to

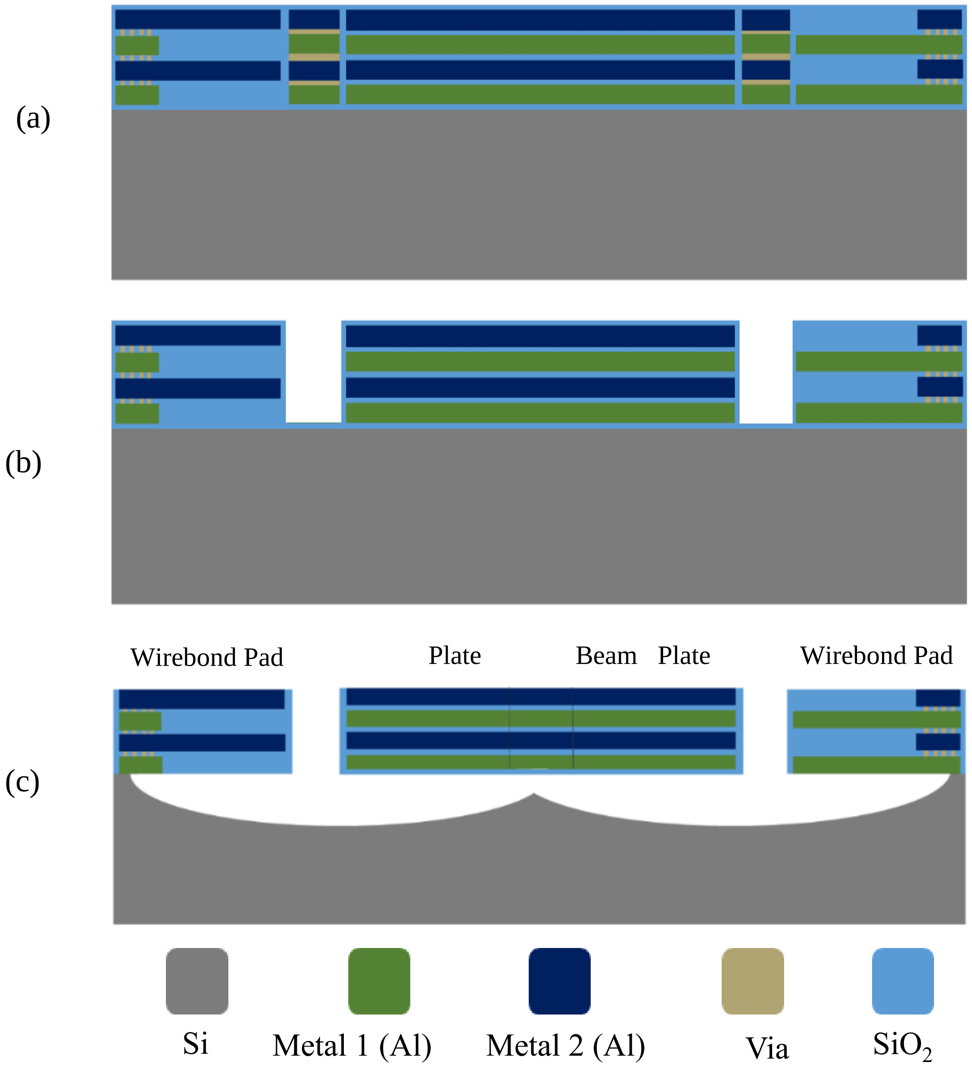

Figure 4.2. Schematic side view showing the post-CMOS mask-less fabrication process flow to form the suspended MEMS structures.

Aluminum and Tungsten respectively making the wet-etch process relatively simple. Following the metal stack etch, the field oxide was then etched by Inductively Coupled Plasma (ICP) as shown in figure 4.2.(b). The thick CMOS passivation layer (~2μm) protects the rest of the chip from the acids and the plasma during the etch steps. Isotropic plasma etching of silicon was then carried out to suspend the resonant structures before removing the passivation oxide (via ICP) to expose the metal wire-bond pads as shown in figure 4.2.(c).

4.1.4 EXPERIMENTAL RESULTS

Figure 4.3.(a). shows a fabricated resonator with two 40×40µm^2 plates connected by a narrow 5×0.5µm^2 beam in the middle. To operate the resonators, a DC bias current along with an AC actuation current were applied to the actuation port, while the readout piezoresistor was biased

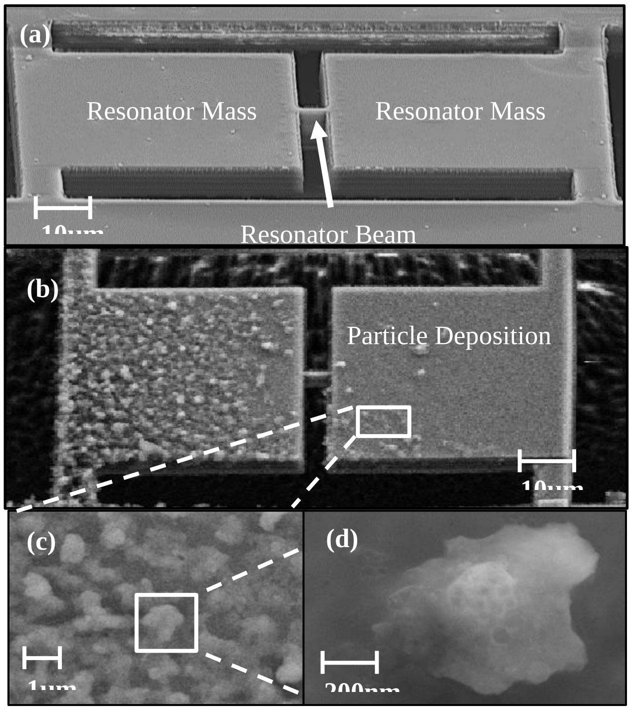

Figure 4.3.(a) SEM views of the CMOS-MEMS metal-oxide resonator.
(b) SEM view of the same resonator after deposition of particles.
(c) (d) Zoomed-in views of the deposited particles.

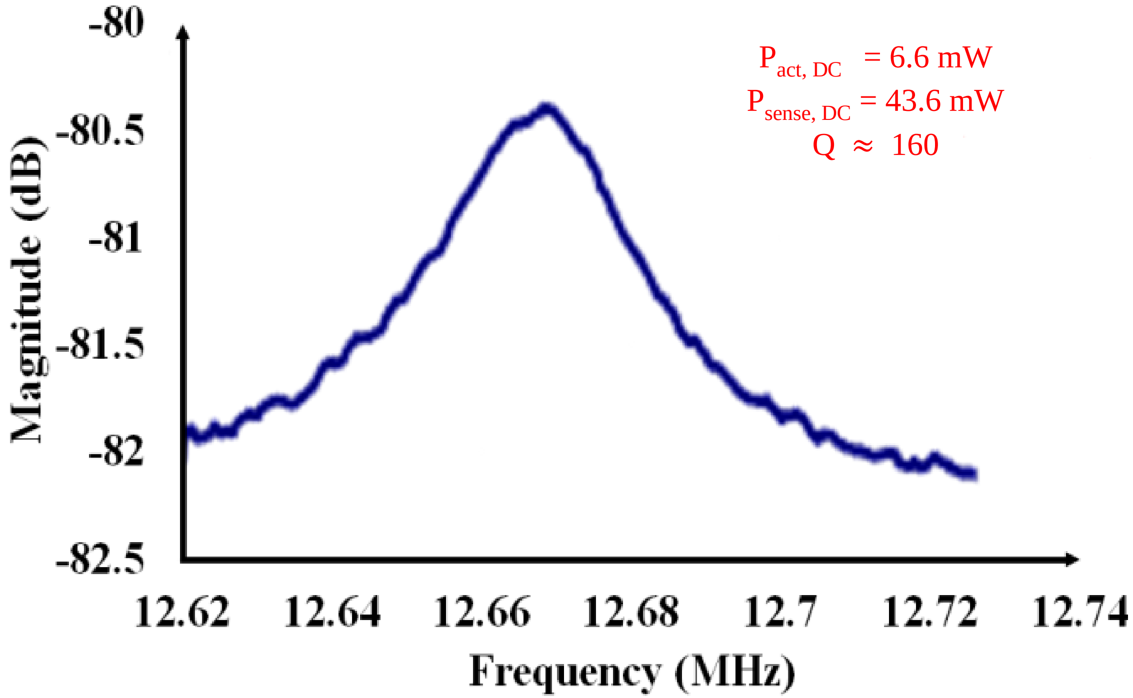

Figure 4.4. Measured frequency response of the CMOS integrated metal-oxide resonator.

with a second DC bias current. Figure 4.4. shows an example of a measured resonance response for the resonator of figure 4.3.(a). First, the resonator has been embedded in the first stage of aerosol impactors [8]. While, frequency of the resonator was monitored over 20-minute periods in regular laboratory air and at the output of an air purifier. In this case, particles with larger sizes have been deposited on the suspended plates of the device shown in figure 4.3.(b).

Figure 4.3.(c). and (d). shows the smaller particle collection on the same device at the output of the air purifier in the turbo mode. In this case, device has been embedded in the second stage of aerosol impactor and the frequency of resonator was monitored over the same time frame. Figure 4.5.(a). shows the collected frequency data over time for different environments including the laboratory, outlet of the air purifier and the outlet of air purifier in turbo mode. Figure 4.5.(b).

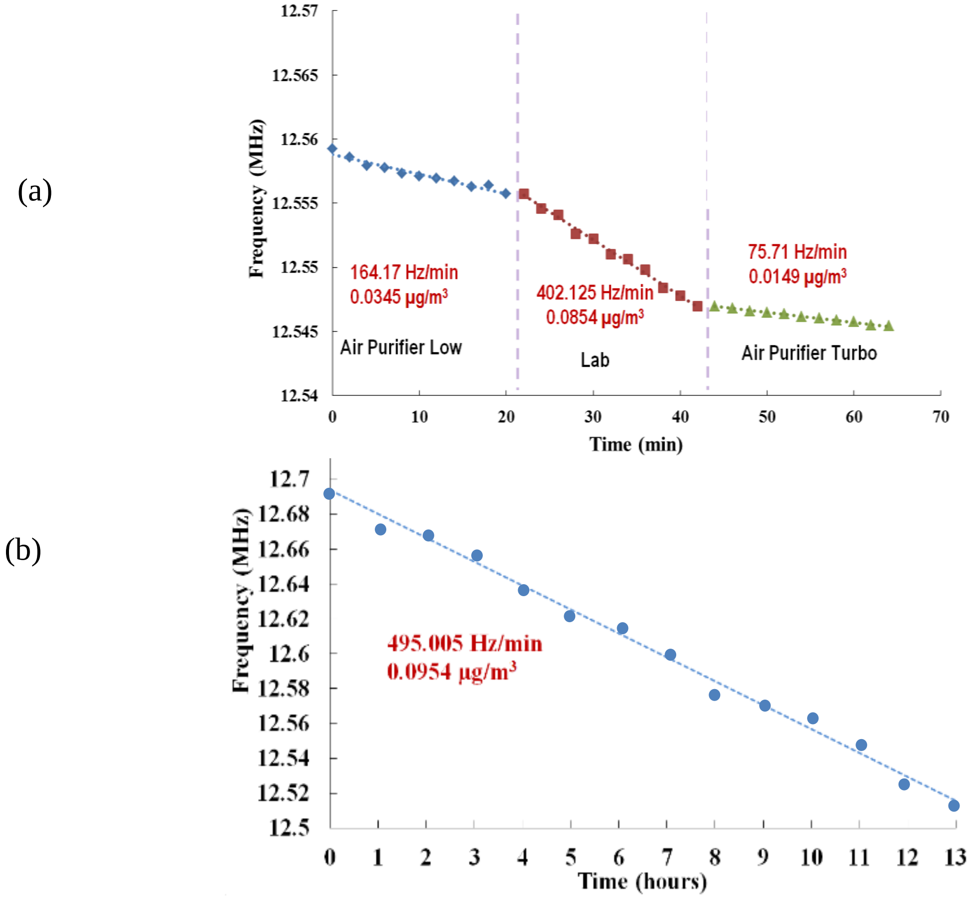

Figure 4.5. Measured change in resonance frequency of the resonant mass balances over time during exposure to airborne particles collected from air samples in different environments. (b) Sensor response during an overnight 13 hours test in regular lab air.

shows sensor response during an overnight 13 hours test in the regular lab environment. Clear changes in the rate of frequency change in accordance with the expected particulate mass levels in different air samples, shows the potential of such sensors for real-time monitoring of airborne particle mass concentrations. Based on the measurements and calculated resonator mass sensitivity of 15.7Hz/pg, the particulate mass concentrations in different air samples are calculated to be ranging from 0.084μg/m^3 for regular laboratory air to 0.014μg/m^3 for air purifier output (for particles with 35-435nm diameter collected in the 2nd stage). TCF of -2.7 ppm/°C was measured for a similar resonator (Figure 4.6.), which is ~10X better than silicon resonator, thanks to the positive temperature coefficient of Young's modulus of silicon dioxide.

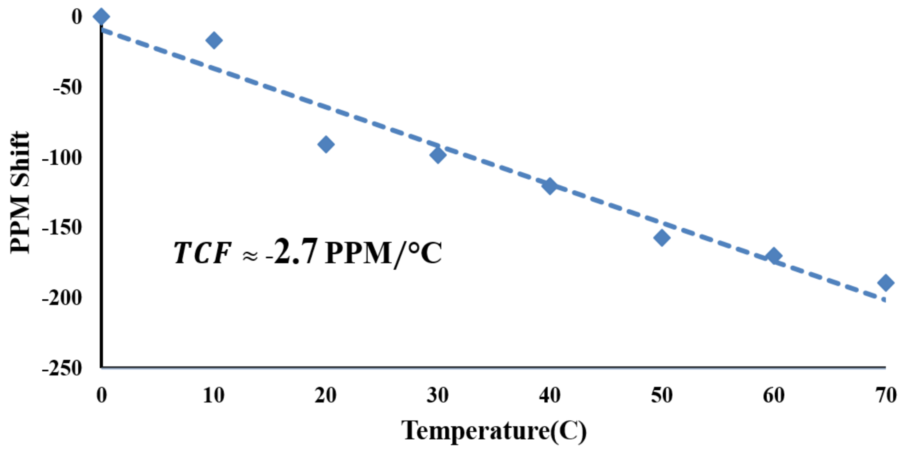

Figure 4.6. Temperature drift characteristics for the 12.6-MHz CMOS integrated metal-oxide resonator

4.1.5 CONCLUSION

CMOS-MEMS resonators have a great potential to be used in wide variety of sensory applications, due to their ease of fabrication. In this work, a thermally actuated metal resonator with piezoresistive readout fabricated on a CMOS chip was demonstrated as a PM monitoring application.

REFERENCES

[1] Layton, Thomas M. Adams Richard A. "Introductory MEMS: Fabrication And Applications."

[2] Busch-Vishniac I (1998) Electromechanical Sensors and Actuators, Springer, New York.

[3] Beeby S, Ensell G, Kraft M, White N (2004) MEMS Mechanical Sensors, Artech House, Inc., Norwood, MA.

[4] Bryzek J, Roundy S, Bircumshaw B, Chung C, Castellino K, Stetter JR, Vestel M (2007) Marvelous MEMS, IEEE Circuits and Devices Magazine, Mar/Apr, pp 8-28.

[5] Maluf N, Williams K (2004) An Introduction to Microelectromechanical Systems Engineering, 2nd edn., Artech House, Inc., Norwood, MA.

[6] Y Lu, Y Wei, L Liu, J Zhang, L Sun, Y Liu, "Towards unsupervised physical activity recognition using smartphone accelerometers," Multimedia Tools and Applications, April 2017

[7] Hernandez, Wilmar. "Robust multivariable estimation of the relevant information coming from a wheel speed sensor and an accelerometer embedded in a car under performance tests." Sensors 5, no. 11 (2005): 488-508.

[8] Park, Dong Hyun, Sojin Shin, and Yeong K. Kim. "Module packaging effects on MEMS airbag sensor performance for automobiles." Microelectronics Reliability 79 (2017): 328-335.

[9] C. Saiprasert, T. Pholprasit, S. Thajchayapong, "Detection of Driving Events using Sensory Data on Smartphone" International Journal of Intelligent Transportation Systems Research, 2017, Volume 15.

[10] Kamada, Yudai, Atsushi Isobe, Takashi Oshima, Yuki Furubayashi, Tatemi Ido, and Tomonori Sekiguchi. "Capacitive MEMS accelerometer with perforated and electrically separated mass structure for low noise and low power." Journal of Microelectromechanical Systems 28, no. 3 (2019): 401-408.

[11] Gesing, A. L., F. D. P. Alves, S. Paul, and J. A. Cordioli. "On the design of a MEMS piezoelectric accelerometer coupled to the middle ear as an implantable sensor for hearing devices." Scientific reports 8, no. 1 (2018): 1-10.

[12] Gupta, Pranav, Mohammad J. Moghimi, Yaesuk Jeong, Divya Gupta, Omer T. Inan, and Farrokh Ayazi. "Precision wearable accelerometer contact microphones for longitudinal monitoring of mechano-acoustic cardiopulmonary signals." NPJ digital medicine 3, no. 1 (2020): 1-8.

[13] Mukhiya, R., P. Agarwal, S. Badjatya, M. Garg, P. Gaikwad, S. Sinha, A. K. Singh, and R. Gopal. "Design, modelling and system level simulations of DRIE-based MEMS differential capacitive accelerometer." Microsystem Technologies 25, no. 9 (2019): 3521-3532.

[14] X. Zhou, L. Che, S. Liang, Y. Lin, X. Li, Y. Wang, “Design and fabrication of a MEMS capacitive accelerometer with fully symmetrical double-sided H-shaped beam structure”, Nicroelectronic Engineering, pp51-57, 2015.

[15] Y. Wang, H. Ding, X. Le, W. Wang, J. Xie, “A MEMS piezoelectric in-plane resonant accelerometer based on aluminum nitride with two-stage microleverage mechanism, Sensors and Actuators, Volume 254, 1 February 2017.

[16] Shen, Zhiyuan, Chin Yaw Tan, Kui Yao, Lei Zhang, and Yi Fan Chen. "A miniaturized wireless accelerometer with micromachined piezoelectric sensing element." Sensors and Actuators A: Physical 241 (2016): 113-119.

[17] k. Hari, S. Kumar, I.R. Praveen, V. Seena, “Out-of-plane dual flexure MEMS piezoresistive accelerometer with low cross axis sensitivity” Microsystem Technologies, 2017

[18] Han, Jianqiang, Zhengqian Zhao, Wenju Niu, Rongyu Huang, and Lizhen Dong. "A low cross-axis sensitivity piezoresistive accelerometer fabricated by masked-maskless wet etching." Sensors and Actuators A: Physical 283 (2018): 17-25.

[19] V. Kumar, X. Guo, S. Pourkamali, “Single-Mask Field Emission based tunable MEMS Tunneling Accelerometer,”, in Press, IEEE Nano, 2015.

[20] Yazdi, Navid, Farrokh Ayazi, and Khalil Najafi. "Micromachined inertial sensors." Proceedings of the IEEE 86, no. 8 (1998): 1640-1659.

[21] Hernando, Carlos, Carla Hernando, Ignacio Martinez-Navarro, Eladio Collado-Boira, Nayara Panizo, and Barbara Hernando. "Estimation of energy consumed by middle-aged recreational marathoners during a marathon using accelerometry-based devices." Scientific Reports 10, no. 1 (2020): 1-10.

[22] Migueles, Jairo H., Cristina Cadenas-Sanchez, Alex V. Rowlands, Pontus Henriksson, Eric J. Shiroma, Francisco M. Acosta, Maria Rodriguez-Ayllon et al. "Comparability of accelerometer signal aggregation metrics across placements and dominant wrist cut points for the assessment of physical activity in adults." Scientific Reports 9, no. 1 (2019): 1-12.

[23] Mahadevan, Nikhil, Charmaine Demanuele, Hao Zhang, Dmitri Volfson, Bryan Ho, Michael Kelley Erb, and Shyamal Patel. "Development of digital biomarkers for resting tremor and bradykinesia using a wrist-worn wearable device." npj Digital Medicine 3, no. 1 (2020): 1-12.

[24] Lee, Dasheng. "Wireless and powerless sensing node system developed for monitoring motors." Sensors 8, no. 8 (2008): 5005-5022.

[25] B.V. Amini and F. Ayazi, “A 2.5V 14-bit Sigma-Delta CMOSSOI Capacitive Accelerometer,” J. SSC, Dec. 2004, pp. 2467-2476.

[26] T. Kobayashi, H. Okada, T. Masuda, R. Maeda, and T. Itoh, “ A digital output accelerometer using MEMS-based piezoelectric accelerometers and arrayed CMOS inverters with satellite capacitors,” Smart Materials and Structures, Volume 20, Number 6, 2011.

[27] Kumar, Varun, Xiaobo Guo, and Siavash Pourkamali. "Single-mask field emission based tunable MEMS tunneling accelerometer." In 2015 IEEE 15th International Conference on Nanotechnology (IEEE-NANO), pp. 755-758. IEEE, 2015.

[28] Kumar, Varun, Roozbeh Jafari, and Siavash Pourkamali. "Ultra-low power digitally operated tunable MEMS accelerometer." IEEE Sensors Journal 16, no. 24 (2016): 8715-8721.

[29] A. Abbasalipour, V. Kumar, R. Jafari, S. Pourkamali, "A 5-Bit Digitally Operated MEMS Accelerometer", Solid-State Sensors, Actuators and Microsystems Workshop Hilton Head Island, South Carolina, June 3-7, 2018.

[30] M. Karpelson, Gu-Yeon Wei and R. J. Wood, "A review of actuation and power electronics options for flapping-wing robotic insects," 2008 IEEE International Conference on Robotics and Automation, Pasadena, CA, 2008, pp. 779-786

[31] Lal, Amit. "Silicon-based ultrasonic surgical actuators." In Proceedings of the 20th Annual International Conference of the IEEE Engineering in Medicine and Biology Society. Vol. 20 Biomedical Engineering Towards the Year 2000 and Beyond (Cat. No. 98CH36286), vol. 6, pp. 2785-2790. IEEE, 1998.

[32] X.Liu,K. Kim, & Y.Sun (2007). A MEMS stage for 3-axis nanopositioning. Journal of Micromechanics and Microengineering, 17(9), 1796

[33] R. C. Gutierrez, T. K. Tang, R. Calvet, E. R. Fossum, "MEMS digital camera," Proc. SPIE 6502, Digital Photography III, 65020K (20 February 2007);

[34] Bell, Dominik J., T. J. Lu, Norman A. Fleck, and Simon M. Spearing. "MEMS actuators and sensors: observations on their performance and selection for purpose." Journal of Micromechanics and Microengineering 15, no. 7 (2005): S153.

[35] Shim, Yonghyun. "Fully Integrated High-Performance MEMS Lumped Element Filters for Reconfigurable Radios." PhD diss., 2013.

[36] Bell, Dominik J., T. J. Lu, Norman A. Fleck, and Simon M. Spearing. "MEMS actuators and sensors: observations on their performance and selection for purpose." Journal of Micromechanics and Microengineering 15, no. 7 (2005): S153.

[37] Liu, Daniel Kuang-Chen, James Friend, and Leslie Yeo. "A brief review of actuation at the micro-scale using electrostatics, electromagnetics and piezoelectric ultrasonics." Acoustical Science and Technology 31, no. 2 (2010): 115-123.

[38] Henderson, D. A. "Micro-scale smart actuator modules for imaging systems." In Proc. ACTUATOR, pp. 266-269. 2012.

[39] C.Liu, “Electrostatic actuation,” in Proc. 2nd Found. MEMS, 2005, pp. 127–168.

[40] Carr, Emily, Scot Olivier, and Olav Solgaard. "Large-stroke self-aligned vertical comb drive actuators for adaptive optics applications." In Mems/Moems Components and Their Applications Iii, vol. 6113, p. 61130T. International Society for Optics and Photonics, 2006.

[41] Hou, Max Ti-Kuang, Gordon Kou-Wei Huang, Jing-Yi Huang, Ke-Min Liao, Rongshun Chen, and Jer-Liang Andrew Yeh. "Extending displacements of comb drive actuators by adding secondary comb electrodes." Journal of micromechanics and microengineering 16, no. 4 (2006): 684.

[42] Yeh, Richard, Seth Hollar, and Kristofer SJ Pister. "Single mask, large force, and large displacement electrostatic linear inchworm motors." Journal of Microelectromechanical Systems 11, no. 4 (2002): 330-336.

[43] Penskiy, I., and S. Bergbreiter. "Optimized electrostatic inchworm motors using a flexible driving arm." Journal of Micromechanics and Microengineering 23, no. 1 (2012): 015018.

[44] Nathanson, Harvey C., William E. Newell, Robert A. Wickstrom, and J. Ransford Davis. "The resonant gate transistor." IEEE Transactions on Electron Devices 14, no. 3 (1967): 117-133.

[45] A. J. Wallash, and L. Levit, “Electrical breakdown and ESD phenomena for devices with nanometer to micron gaps,” proceedings of SPIE, Micromachining and Microfabrication, 2003, pp. 87-96

[46] Rollier, A. S., Bernard Legrand, D. Collard, and L. Buchaillot. "The stability and pull-in voltage of electrostatic parallel-plate actuators in liquid solutions." Journal of Micromechanics and microengineering 16, no. 4 (2006): 794.

[47] Felder, E. Lee and D. L. DeVoe, "Large Vertical Displacement Electrostatic Zipper Microstage Actuators," in Journal of Microelectromechanical Systems, vol. 24, no. 4, pp. 896-903, Aug. 2015.

[48] Chen, Ssu-Han, Aron Michael, and Chee Yee Kwok. "Enhancing out-of-plane stroke in piezoelectrically driven micro-lens actuator with residual stress control." Sensors and Actuators A: Physical 303 (2020): 111620.

[49] Ba-Tis, Faez, and Ridha Ben-Mrad. "A 3-DOF MEMS electrostatic piston-tube actuator." Journal of Microelectromechanical Systems 24, no. 4 (2015): 1173-1184.

[50] Conrad, Holger, Harald Schenk, Bert Kaiser, Sergiu Langa, Matthieu Gaudet, Klaus Schimmanz, Michael Stolz, and Miriam Lenz. "A small-gap electrostatic micro-actuator for large deflections." Nature communications 6, no. 1 (2015): 1-7.

[51] Varun Kumar, “Novel Sensing Approaches Towards Ultimate Mems Sensors”. Dissertation University of Texas at Dallas, 2018

[52] D. B. Heinz, V. A. Hong, C. H. Ahn, E. J. Ng, Y. Yang and T. W. Kenny, "Experimental Investigation Into Stiction Forces and Dynamic Mechanical Anti-Stiction Solutions in Ultra-Clean Encapsulated MEMS Devices," in Journal of Microelectromechanical Systems, vol. 25, no. 3, pp. 469-478, June 2016.

[53] Panchen, 1889 Wied. Ann 37, pp. 69-96.

[54] P. L. Chapman and P. T. Krein, “Micromotor technology: electric drive designer’s perspective,” in Conference Record of the 2001 IEEE Industry Applications Conference, 2001. Thirty-Sixth IAS Annual Meeting, 2001, vol. 3, pp. 1978–1983 vol.3.

[55] A. J. Wallash, and L. Levit, “Electrical breakdown and ESD phenomena for devices with nanometer to micron gaps,” proceedings of SPIE, Micromachining and Microfabrication, 2003, pp. 87-96.

[56] S. Pourkamali, “High Frequency Capacitive Single Crystal Silicon Resonators and Coupled Resonator Systems,” PhD Thesis, Georgia Institute of Technology, 2006.

[57] A. Abbasalipour, P. Palit and S. Pourkamali, "High-Energy Density Micro-Machined Cellular Arrays of Electrostatic Actuators," 2019 20th International Conference on Solid-State Sensors, Actuators and Microsystems & Eurosensors XXXIII (TRANSDUCERS & EUROSENSORS XXXIII), Berlin, Germany, 2019, pp. 1870-1873.

[58] A-S. Rollier, B. Legrand, D. Collard, and L. Buchaillot, "The stability and pull-in voltage of electrostatic parallel-plate actuators in liquid solutions," Journal of Micromachining and Microengineering, 16, 2006, pp. 794-801.

[59] A.K. Samarao and F. Ayazi, "Self-polarized capacitive silicon micromechanical resonators via charge trapping," IEEE International Electron Devices Meeting (IEDM 2010), San Francisco, CA, Dec. 2010, pp. 741-744.

[60] A. D. Kappos et al., “Health effects of particles in ambient air,” Int. J. Hygiene Environ. Health, vol. 207, pp. 399–407, Sep. 2004.

[61] M. Tamaoki, K. Nishiki, A. Shimazaki, Y. Sasaki, and S. Yanagi, “The effect of airborne contaminants in the cleanroom for ULSI manufacturing process,” in Proc. IEEE/SEMI Adv. Semiconductor Manuf. Conf. Workshop, (ASMC), Apr. 1995, pp. 322–326.

[62] H.-S. Moon, Y.-W. Nam, J. C. Park, and H.-I. Jung, “Dielectrophoretic separation of airborne microbes and dust particles using a microfluidic channel for real-time bioaerosol monitoring,” Environ. Sci. Technol., vol. 43, pp. 5857–5863, Sep. 2009.

[63] D. J. Collins, T. Alan, and A. Neild, “Particle separation using virtual deterministic lateral displacement (vDLD),” Lab Chip, vol. 14, no. 9, p. 1595, 2014.

[64] S. Choi and J.-K. Park, “Continuous hydrophoretic separation and sizing of microparticles using slanted obstacles in a microchannel,” Lab Chip, vol. 7, pp. 890–897, Apr. 2007.

[65] A. E. Carruthers, J. S. Walker, A. Casey, A. J. Orr-Ewing, and J. P. Reid, “Selection and characterization of aerosol particle size using a Bessel beam optical trap for single particle analysis,” Phys. Chem. Chem. Phys., vol. 14, no. 19, pp. 6741–6748, Apr. 2012.

[66] P. D. Rosenberg et al., “Particle sizing calibration with refractive index correction for light scattering optical particle counters and impacts upon PCASP and CDP data collected during the Fennec campaign,” Atmos. Meas. Tech., vol. 5, no. 5

[67] M. Maldonado -Garcia, V. Kumar, J.C. Wilson, and S. Pourkamali, “Chip-scale implementation and Cascade Assembly of particulate matter Collectors with embedded resonant mass balances”, Accepted for Publication, IEEE Sensors Journal, November 2016. vol. 17 Issue: 6.

[68] E. Mehdizadeh, V. Kumar, J. Gonzales, R. Abdolvand, and S. Pourkamali, “A Two-Stage Aerosol Impactor with Embedded MEMS Resonant Mass Balances for Particulate Size Segregation and Mass Concentration Monitoring”, IEEE Sensors Conference, 2013.

[69] V. Qaradaghi, M. Mahdavi, V. Kumar, S. Pourkamali, “Frequency output mems resonator on membrane pressure sensors”, IEEE Sensors 2016.

[70] V. Qaradaghi, M. Mahdavi, A. Ramezany, and S. Pourkamali, “MEMS Resonant Sensors for Real-Time Thin Film Sheer Stress Monitoring”, In Press, IFCS 2016.

[71] V. Kumar, A. Ramezany, M. Mahdavi, S. Pourkamali, “Amplitude Modulated Lorentz Force MEMS Magnetometer with Pico-tesla sensitivity”, Journal of Micromechanics and Microengineering, Volume 26, Number 10, 105021, September 2016.

[72] A. Abbasalipour, M. Mahdavi, V. Kumar, S. Pourkamali, “Nano-Precision Micromachined Frequency Output Profilometer” IEEE Sensors 2016. pp 1-3, 2016.

[73] E. Mehdizadeh, V. Kumar, J. Wilson, S. Pourkamali, “Inertial Impaction on MEMS Balance Chips for Real-Time Air Quality Monitoring”, IEEE Sensors Journal, Vol. 17, Issue 8, pp 2329-2337, April 2017.

BIOGRAPHICAL SKETCH

Amin Abbasalipour was born in Tehran, Iran. In 2001, he started his undergraduate studies at the Shahid Chamran University of Ahvaz in Electrical Engineering with a focus on electronic circuits and devices. In 2007, he started his master's program in University of Tabriz with a focus on control engineering. In 2014, he joined the Micronexlab at The University of Texas at Dallas to pursue his PhD degree under the supervision and guidance of Dr. Siavash Pourkamali. During his PhD, he took part in a variety of projects related to micro/nanoelectromechanical systems that employed capacitive, thermal, and piezoelectric actuation mechanisms. His specialties include electrostatic high energy density actuators, motional sensors with capacitive transduction, piezoelectric-on-silicon resonators and thermal actuators. His dissertation focused on high energy density and low power electrostatic transducers.

CURRICULUM VITAE

Amin Abbasaliour

Email: e.ramezany@utdallas.edu

PhD candidate in Electrical Engineering, specialized in design, fabrication, and characterization of **Electrostatic low power and high work density MEMS transducers.** at The University of Texas at Dallas under guidance of Dr. Siavash Pourkamali. Main projects include **Arrayed Cellular Electrostatic Actuator, Ultra Low Power Digitally Operated MEMS Accelerometer.**

EDUCATION

Shahid Chamran University, Ahvaz, Iran	Electrical Engineering BS 2006
Tabriz University, Tabriz, Iran	Electrical Engineering MS 2010
University of Texas at Dallas, Dallas, TX	Electrical Engineering PhD 2020

Dissertation: Novel Sensing Approaches towards Ultimate MEMS sensors

The purpose of this research project is to explore novel techniques and approaches for achieving ultra-low power accelerometer and high work density electrostatic MEMS actuator.

Key features of the research**:**

MEMS Accelerometer:

In this work, an electrostatically tunable MEMS acceleration switch and its operation as a 8-bit digital accelerometer hs been demonstrated. Such devices only require bias voltages for operation (zero static power consumption) enabling significant power reduction by eliminating the need for an analog-front-end. The sensor consists of an acceleration switch (proof mass with an output contact electrode) surrounded by sets of electrostatic actuators each corresponding to one bit of the digital binary output. Performing a binary search and activating different actuators in proper order the applied acceleration can be determined. The tested 8-bit prototype shows good agreement between the applied acceleration and sensor output with resolution of 10mg limited by the number of bits, i.e. 1/256 of the full-scale acceleration of 2.7g.

Arrayed Cellular Electrostatic Actuator:

In this work, micro-machined electrostatic actuator arrays capable of producing relatively large forces and wide displacement ranges. The actuators are comprised of a flexible silicon skeleton (mesh) with a network of trench refilling polysilicon electrodes electrically insulated and separated from the silicon walls by submicron airgaps. The array architecture provides flexibility and large displacement by adding displacements from individual cells, while submicron gaps lead to relatively large actuation forces. Out of plane displacement of up to 678µm with actuation force of 1.22mN at the actuator tip has been measured for a 7421 cell (4mm × 2mm) fabricated array with 46V actuation voltage. Also, axial displacement of 20.5 µm with blocking force of 0.9mN at the tip of the device has been achieved for a 2299 cell (2mm × 1mm) fabricated array with 35 actuation voltage.

Courses:

Quantum Physical Electronics, Introduction to MEMS, Lithography and Nanofabrication, Digital Signal Processing, Pattern Recognition, Speech and Speaker Recognition.

Research Experience

The University of Texas at Dallas Fall 2014-Present

Projects Under Supervision of Dr. Siavash Pourkamali

- Design, fabrication, and characterization of **Digitally Operating MEMS Accelerometer** for sensory applications.

- Fabrication characterization of modified HARPS fabrication process using 5 lithography mask.

- Design, fabrication and characterization of **Arrayed Cellular Electrostatic Actuator** as high energy density MEMS actuator.

- Design, fabrication, and characterization of **Thermally Actuated Piezoresisitive Readout resonator** as high precision profilometer and Force probes.

- Design and Fabrication of novel **Electrostatic Motors using silicon substrates with improved specific torque density**.

- Development of a new electromechanical model for Thermal Piezoresistive Amplifiers.

- Design and development of CMOS compatible MEMS resonators in collaboration with Texas Instruments.

- Fabrication and Characterization of **Thin Film Piezoelectric (ALN) on Silicon** as a bulk extensional resonator for sensing applications.

- Fabrication and Characterization of **Thin Film Piezoelectric (ALN) on Silicon** as a ring resonator with high quality factor for liquid phase sensing applications.

SKILLS AND TECHNIQUES

Cleanroom Experience: Photolithography, E-beam evaporation and sputtering, Plasma etch (ICP and DRIE), SEM, E-Beam lithography, and ALD.

Characterization Experience: wire-bonding (wedge and ball bonding), RF probe station, RF PCB design, Network analysis and calibration (including SLOT and TRL), Spectrum analysis (including Noise figure and phase noise measurements)

Software: COMSOL MEMS Module, Cadence, Pspice, Matlab, C/C++**,** L-Edit, and Solid Works

PUBLICATIONS

Journal Papers:

1. M. Mahdavi, **A. Abbasalipour** and S. Pourkamali, "Thin Film Piezoelectric-on-Silicon Elliptical Resonators with Low Liquid Phase Motional Resistances," in IEEE Sensors Journal, vol. 19, no. 1, pp. 113-120, 1 Jan.1, 2019.

4. Mahdavi, M., **Abbasalipour, A.**, Ramezany, A., & Pourkamali, S. (2016). Micromachined Frequency-Output Force Probes. *IEEE Sensors Journal*, *16*(14), 5520-5521.

Conference Papers:

1. **A. Abbasalipour**, P. Palit, S. Pourkamali, “High-Energy Density Micro-Machined Cellular Arrays of Electrostatic Actuators” the 20th International Conference on Solid-State Sensors, Actuators and Microsystems, Transducers June 2019.

2. **A. Abbasalipour**, V. Kumar, S. Pourkamali, “A 5-Bit Digitally Operated MEMS Accelerometer”. Hilton Head Sensors and Actuators workshop, 2018.

3. **A. Abbasalipour**, V. Kumar, A. Ramezany and S. Pourkamali, "Thermal Piezoresistive Resonant Mass Balance Implemented in a Standard CMOS Process," *2018 IEEE International Frequency Control Symposium (IFCS)*, Olympic Valley, CA, 2018, pp. 1-4.

4. V. Kumar, **A. Abbasalipour**, A. Ramezany and S. Pourkamali, "A Low-Power CMOS-MEMS Vibration Spectrum Analyzer," *2018 IEEE International Frequency Control Symposium (IFCS)*, Olympic Valley, CA, 2018, pp. 1-4.

5. M. Mahdavi, H. Wang, **A. Abbasalipour**, W. Hu and S. Pourkamali, "Micro-Resonator-on-Membrane for Real-Time Biosensing," *2018 IEEE International Frequency Control Symposium (IFCS)*, Olympic Valley, CA, 2018, pp. 1-4.

6. **A. Abbasalipour**, M. Mahdavi, V. Kumar, S. Pourkamali, S. Daryadel and M. Minary, "Nano-precision Micromachined Frequency Output Profilometer," *2016 IEEE SENSORS*, Orlando, FL, 2016, pp. 1-3.

7. M. Mahdavi, A. Abbasalipour, A. Moses, and S. Pourkamali, " Resonant Piezoelectric Cantilevers as Nano-Precision Displacement Probes," Hilton Head Sensors and Actuators workshop, 2016.

8. S. Pourkamali, **A. Abbasalipour**, P. Palit, "Micromachined electrostatic actuator arrays with submicron transduction gaps for high energy density and long displacement range." Technology Disclosure, University of Texas at Dallas.